CHAPTER IV
RESULTS AND DISCUSSION

4.1 Catalyst Characterization

4.1.1 Surface Area Measurement (SAA)

All catalysts were analyzed for their surface areas and pore sizes, as shown in Table. 4.1. Under the 3wt% Au deposition, the initial result shows that the Au/CeO_2 and Au/ZrO_2 had the surface areas of 91 and 163 m^2/g, respectively, while the surface areas of $Au/CeO_2–ZrO_2$ catalysts were found in the range of 114-130 m^2/g. This revealed that the addition of Zr to perform the $CeO_2–ZrO_2$ mixed oxide support caused the crystal structure of the ceria lattice, where the Zr^{4+} was able to cooperate inside the Ce^{4+} lattice, resulting in the shrinking in ceria crystallite size together with the increment of ceria surface surface area in the Ce–Zr solid solution, when compared with that of pure CeO_2 support (Masui *et al.*, 1998).

The change in surface area was in agreement with the variation in pore diameter of the support, where the increase in surface area was the consequence of the smaller pore diameter of the Ce–Zr structure. Moreover, the addition of Zr lowered the pore diameter from 96.9 to 31.6-57.8 Å. Among the mixed oxide catalysts, the 50% Zr addition provided the highest surface area (130 m^2/g), while the excess Zr concentration of 75 %mol slightly decreased the surface area. This suggested the expansion of the Ce^{4+} lattice and crystallite size when higher Zr than the optimal amount was added to cause the segregation of Zr^{4+} outside the ceria lattice instead, and then probably stayed remaining on the ceria surface (Grau-Crespo *et al.*, 2011). Consequently, the solid solution formation could not form uniformly at high Zr contents. To support this explanation of solid solution formation, the XRD characterization was necessary to determine the lattice constant and ceria crystallite size, which were discussed later.

Table 4.1 Chemical and physical properties of $Au/CeO_2–ZrO_2$ and $Au–Cu/CeO_2–ZrO_2$ catalysts

Catalyst	Total metal loading (wt%)	Calcination temperature (°C)	BET surface area (m^2/g)	Pore diameter (Å)	Crystallite size[a] (nm)		Lattice constant[b] (nm)		Au (wt%)	Cu (wt%)	Synthesized Au/Cu ratio	Preparation technique[c]
					CeO_2	Au (111)	CeO_2	Au				
Au/CeO_2	3	400	91	96.9	7.60	8.61	0.543	-	2.85	-	-	DP
$Au/Ce_{0.75}Zr_{0.25}O_2$ (CP)	3	400	114	53.5	7.16	3.53	0.543	0.407	2.88	-	-	DCP
$Au/Ce_{0.75}Zr_{0.25}O_2$ (SN)	3	400	131	53.4	7.50	< 5	0.543	-	2.71	-	-	DSN
$Au/Ce_{0.5}Zr_{0.5}O_2$	3	400	130	57.8	6.22	< 5	0.542	-	2.55	-	-	DCP
$Au/Ce_{0.25}Zr_{0.75}O_2$	3	400	127	31.6	4.16	11.92	0.517	-	2.17	-	-	DCP
Au/ZrO_2	3	400	163	34.1	-	4.79	-	-	1.57	-	-	DP
$3Au1Cu/Ce_{0.75}Zr_{0.25}O_2$	3	400	132	45.3	6.95	5.98	0.542	0.408	2.61	0.23	3.66	DCP
$1Au1Cu/Ce_{0.75}Zr_{0.25}O_2$	3	400	125	41.5	7.17	< 5	0.542	0.409	2.28	0.73	1.01	DCP
$1Au3Cu/Ce_{0.75}Zr_{0.25}O_2$	3	400	123	39.8	5.96	< 5	0.542	0.409	1.45	1.46	0.32	DCP
$Cu/Ce_{0.75}Zr_{0.25}O_2$	3	400	135	39.0	7.77	-	0.542	-	-	3.05	-	DCP
$3Au1Cu/Ce_{0.75}Zr_{0.25}O_2$	5	400	125	46.3	6.53	5.10	0.542	-	4.30	0.46	3.02	DCP
$3Au1Cu/Ce_{0.75}Zr_{0.25}O_2$	5	300	143	51.1	5.95	4.92	0.543	-	4.45	0.48	2.98	DCP
$3Au1Cu/Ce_{0.75}Zr_{0.25}O_2$	5	200	148	37.1	7.56	5.11	0.541	-	4.12	0.48	2.76	DCP
$3Au1Cu/Ce_{0.75}Zr_{0.25}O_2$	7	400	136	38.0	7.31	5.96	0.540	-	5.60	0.64	2.85	DCP

[a] Mean ceria crystallite sizes were calculated from the average values of CeO_2 (111), (200), (220), and (311), while the Au crystallite sizes were calculated from the Au (111).

[b] Unit cell parameter calculated from CeO_2 (111) with Bragg's equation.

[c] DP = Deposition–precipitation, DCP = Deposition–coprecipitation, DSN = Deposition–sonochemical.

When comparing the routes of $Ce_{0.75}Zr_{0.25}O_2$ support preparation between co–precipitation (CP) and sonochemical (SN), it seemed that the surface area of SN catalyst gave higher surface area (131 m^2/g) than that of CP one (114 m^2/g). Tu and coworkers (2009) have reported that the ultrasonic pretreatment technique provided higher surface area and smaller pore diameter of the support site. However, our catalysts with different preparation techniques did not show the change in pore diameter of ~ 53 Å.

When applying the co–addition of copper metal to perform bimetallic Au–Cu catalysts under the same 3 wt% loading. The addition of copper metal helped to increase the surface area of catalyst from 114 m^2/g to 123-132 m^2/g, which was in accordance with Mozer and coworkers, (2009). It is clearly seen that the use of the lowest copper concentration (Au/Cu = 3/1 or $3Au1Cu/Ce_{0.75}Zr_{0.25}O_2$) gave the highest surface area, while the higher copper contents (Au/Cu = 1/1 and 1/3) decreased the surface area of catalysts. The variation of total metal loading (3–7 wt%) over the bimetallic catalysts was investigated, but the trend of surface area was fluctuated and did not follow the same trend, where the 5 wt% loading present the lowest area of 125 m^2/g. When varying the calcination temperature over the 5 wt% catalyst, the increment of surface area became pronounced after lowering the calcination temperature than 400 °C, respectively.

4.1.2 X-ray Diffraction (XRD)

Figure 4.1A shows the XRD patterns of CeO_2, ZrO_2, and 3 wt% $Au/CeO_2–ZrO_2$. CeO_2 support present a strong diffraction peak at $2\theta = 28.5°$, which was assigned to a typical cubic fluorite structure of plane (111). Other peaks at 33.08, 47.47, 56.33, 59.08, 69.40, 76.69, and 79.07° were corresponded to the planes (200), (220), (311), (222), (400), (331), and (420) for CuKα (1.5406 Å) radiation, respectively (Jia *et al.*, 2008). For pure ZrO_2 support, the diffraction peaks at 30°, 34.5°, 50°, and 60° were attributed with the tetragonal structure, whereas the peaks at 24°, 28°, 32°, and 41° was assigned to monoclinic structure (Bi *et al.*, 2007). The CeO_2 diffraction peaks became broader with lower intensity and shifted to higher angles after adding the Zr metal. The diffraction peaks of ZrO_2 were not observed up to a ZrO_2 content of 50%, which suggested the incorporation of Zr^{4+} into Ce^{4+} lattice to form a solid solution. This was due to the shrinkage of lattice structure with the replacement of cerium cation (Ce^{4+}) by zirconium cation (Zr^{4+}) to generate the solid solution (Biswas *et al.*, 2007). This could be implied that the Zr^{4+} ions could partially segregate from the Ce^{4+} lattice during forming the solid solution when the amount of Zr used was above the solubility limit in ceria lattice. This can be another measurement to define the homogeneity of uniform solid solution phase. Besides, the crystallite and lattice constant of CeO_2 were also calculated, as shown in Table 1. It was clearly seen that the decrease in the mean CeO_2 crystallite size with the Zr addition (from 7.6 to 4.16 nm) was an evidence for the formation of $CeO_2–ZrO_2$ solid solution phase (Biswas *et al.*, 2007), which was in line with the increment of the BET surface area (Kambolis *et al.*, 2010). Furthermore, the shifting behavior of CeO_2 planes towards higher angles led to the decrease the CeO_2 lattice constant (a_o), calculated from the Bragg's equation, from 0.543 to 0.517 nm. This was reasonable to the insertion of smaller Zr^{4+} (0.84 Å) ions into Ce^{4+} (0.97 Å) lattice in order to form solid solution (Ratnasamy *et al.*, 2004). Therefore, it was reasonable to conclude that the most uniform solid solution was occurred at $Ce_{0.75}Zr_{0.25}O_2$, which had no observation of ZrO_2 diffraction, implying the well–dispersed ZrO_2 particles inside the ceria crystal structure (Biswas *et al.*, 2007). The peak intensity of Au(111) at 38.46° was observed in all samples (Gamboa-Rosales *et al.*, 2012); however, it was difficult to calculate the Au crystallite size of $Au/Ce_{0.5}Zr_{0.5}O_2$ catalyst because of

its very broad peak, suggesting that (i) the small Au nanoparticles was well-dispersed on the support surface or (ii) the gold particle size was below the XRD detection limit of 5 nm (Liao *et al.*, 2013).

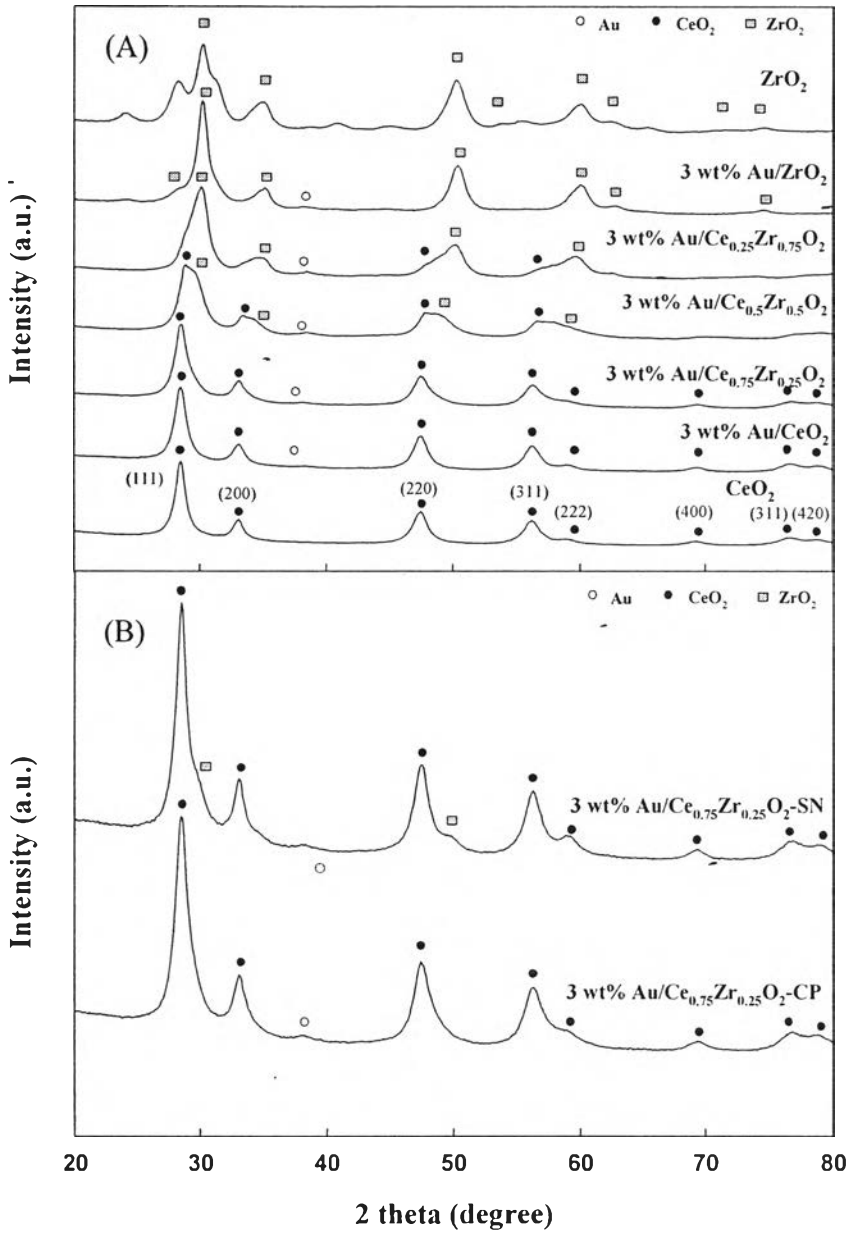

Figure 4.1 XRD patterns of 3 wt% Au/CeO_2-ZrO_2 catalysts calcined at 400 °C: (A) Effect of support composition (Ce/(Ce+Zr) atomic ratio). (B) Effect of support preparation techniques; co–precipitation (CP), and sonochemical (SN).

When focusing on the CP and SN catalysts, as shown in Figure 4.1B, all ceria diffractions showed no shifting behavior between these two catalysts. Interestingly, the peak intensity of SN sample was higher than that of CP sample, which related to the increase in CeO_2 crystallite size (Kambolis *et al.*, 2010), and the existence of some ZrO_2 diffractions (29° and 49°) were also observed in SN sample. The possible explanation was linked with the lack of CeO_2–ZrO_2 solid solution phase, where the segregated ZrO_2 particles possibly stayed remaining on the ceria surface within with the expansion of ceria crystallite size (Kaspar *et al.*, 2003). So, the XRD detection of CeO_2 and ZrO_2 crystals over the SN catalyst surface was possible.

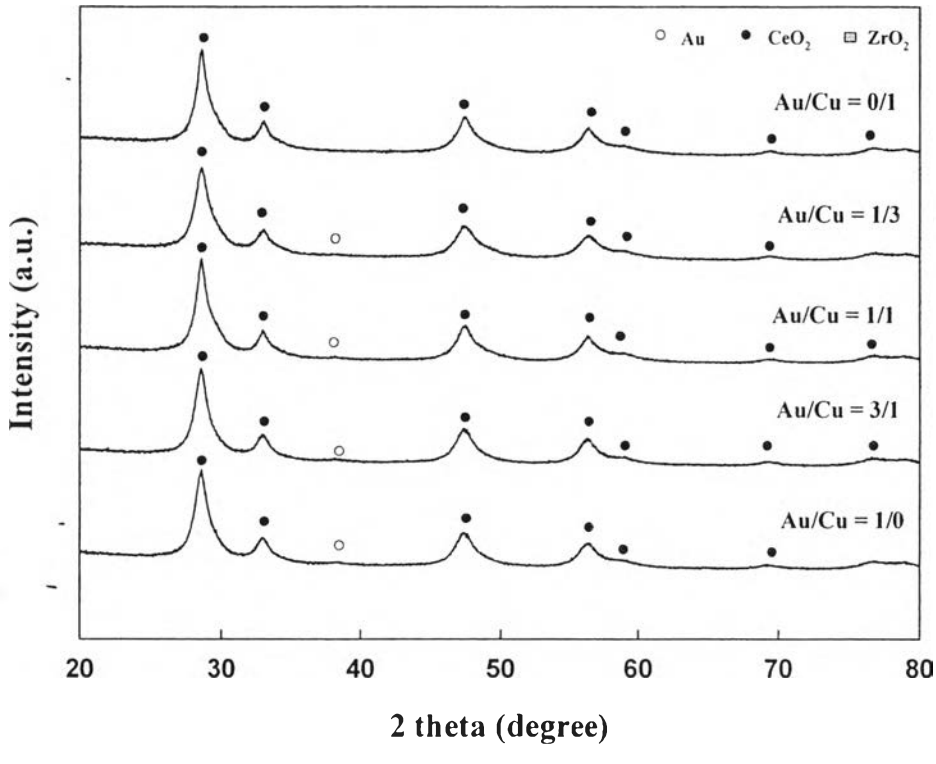

Figure 4.2 XRD patterns of 3 wt% Au–Cu/$Ce_{0.75}Zr_{0.25}O_2$ catalysts with various Au/Cu atomic ratios.

For the XRD patterns of the bimetallic catalysts (Figure 4.2), the bimetallic catalysts show the same XRD patterns as that of $Au/Ce_{0.75}Zr_{0.25}O_2$ catalyst. None of copper diffraction was observed on the bimetallic catalysts due to the highly dispersed copper or CuO nanoparticles on the catalyst surface. Even though the Au diffractions were observed, their intensities were too low to calculate the crystallite size except 3Au1Cu catalyst (5.98 nm). It has been reported previously the effect of copper addition on the synergistic effect of Au crystallite size, where only small amount of copper could prevent the agglomeration of Au nanoparticles (Liu *et al.*, 2011). Among the bimetallic catalysts, the small deviation of the mean CeO_2 crystallite size was observed in the range of 5.96–7.17 nm, indicating less effect of Cu addition on support site. Taking into account the zoom-in Au diffraction in Figure 4.3, the Au (111) became shifting toward lower angle (38.32° to 38.12°) after adding the copper content from Au/Cu = 1/0 to Au/Cu = 1/3, respectively. This was known as another indicator of Au–Cu alloy formation, which was in line with many literatures (Liu *et al.*, 2011). With this initial observation, the addition of Cu was able to prevent the Au agglomeration and form the Au–Cu alloy nanoparticles.

Table 4.2 Crystallite sizes of the $Au–Cu/Ce_{0.75}Zr_{0.25}O_2$ catalysts after exposure to the reaction at 350 °C for 21 hours

Au/Cu Atomic ratio	Crystallite size (nm)				
	$CeO_2(111)$	$CeO_2(200)$	$CeO_2(220)$	$CeO_2(311)$	Au(111)
Au/Cu = 1/0	8.3	9.8	7.1	6.7	8.4
Au/Cu = 3/1	8.4	8.2	7.0	6.7	6.3
Au/Cu = 0/1	9.0	11.1	7.2	7.7	-

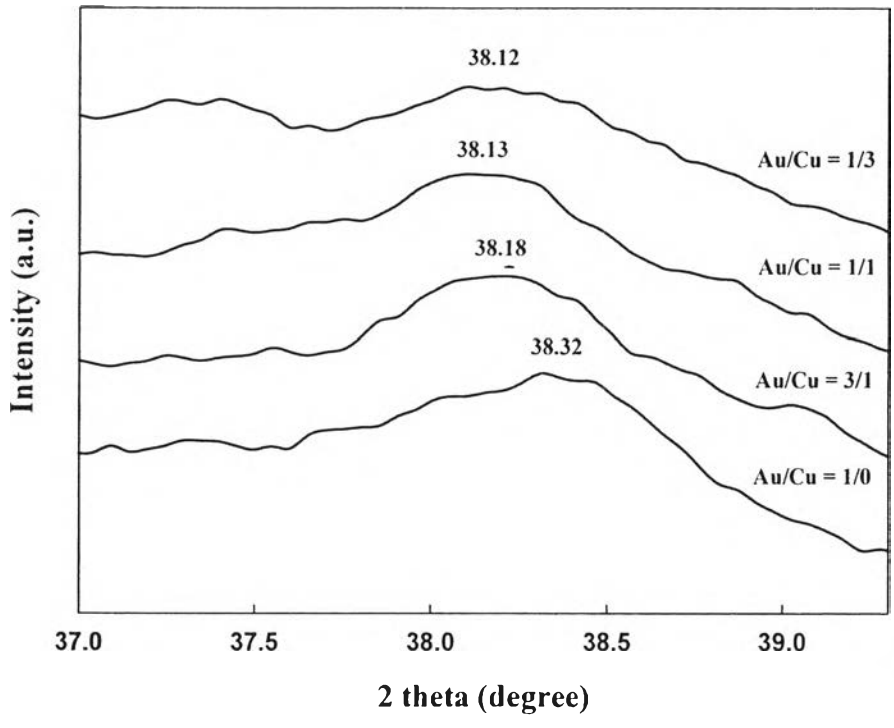

Figure 4.3 XRD patterns of the Au diffractions in the Au–Cu/$Ce_{0.75}Zr_{0.25}O_2$ catalysts with various Au/Cu atomic ratios.

Figure 4.4A shows the XRD patterns of the spent Au–Cu/$Ce_{0.75}Zr_{0.25}O_2$ catalysts with different Au/Cu atomic ratios after exposure to the OSRM reaction. From these patterns, the Au (111) diffractions became more visible with the growth in crystallite size of 8.4 and 6.3 nm for pure Au and 3Au1Cu catalysts, respectively, and the mean CeO_2 crystallite sizes were increased to 7.6–8.8 nm. This represented the change in synergistic effect on both alloy site and support site as well.

When increasing the total metal loading from 3 wt% to 7 wt% over the 3Au1Cu/$Ce_{0.75}Zr_{0.25}O_2$, as shown in Figure 4.4B, the Au (111) or likely Au–Cu alloy diffractions became more pronounced at higher loading, attributing to the increasing in alloy crystallite size. Even being calcined with different temperatures (Figure 4.5), there was no difference in the XRD patterns of 5 wt% 3Au1Cu

catalysts, where the mean crystallite sizes of CeO_2 in all samples were found in the range of 5.95–7.56 nm, which referred to the small growth in support crystallinity.

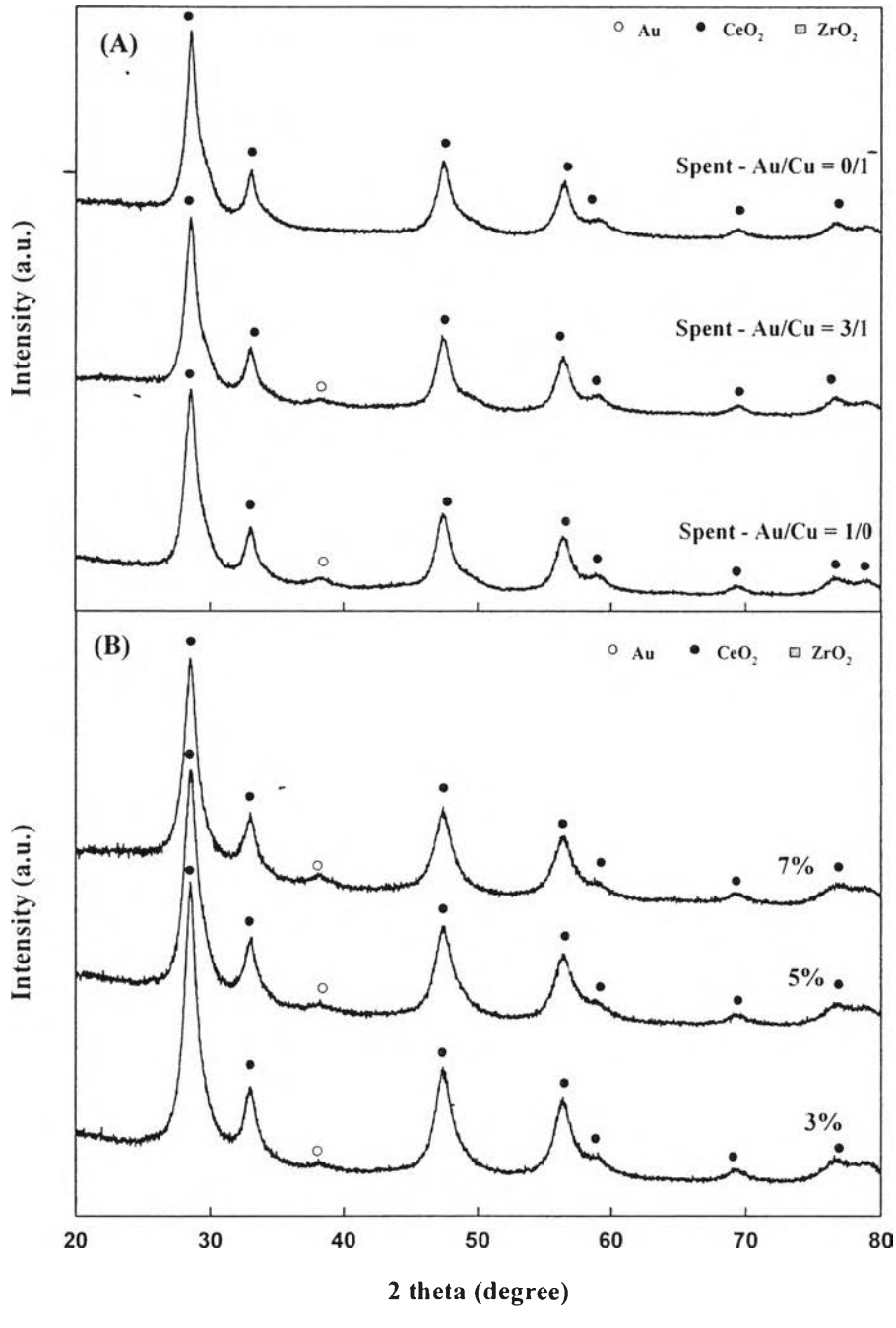

Figure 4.4 XRD patterns of (A) spent Au–Cu/$Ce_{0.25}Zr_{0.75}O_2$ catalysts with different Au/Cu atomic ratios after exposure to reaction at 350 °C for21 hours. (B) Effect of total metal loading on 3Au1Cu/$Ce_{0.25}Zr_{0.75}O_2$.

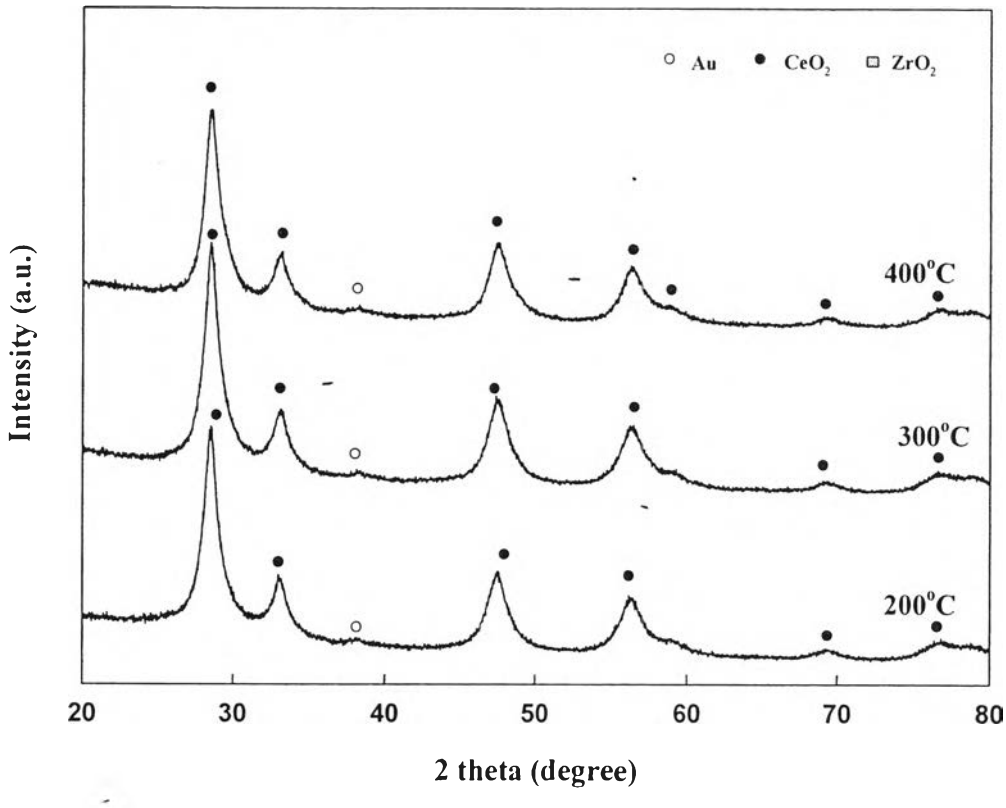

Figure 4.5 XRD patterns of 5 wt% 3Au1Cu/$Ce_{0.75}Zr_{0.25}O_2$ catalysts with different calcination temperatures.

4.1.3 Temperature-programmed Reduction (TPR)

According to the TPR profiles of $Au/CeO_2–ZrO_2$ catalysts in Figure 4.6A, the CeO_2 support shows two peaks; the low–temperature peak at 470 °C was assigned to the reduction of surface oxygen species, and the high–temperature peak at 839 °C was attributed to the reduction of bulk oxygen from the ceria structure (Andreeva *et al.*, 2002). There was no reduction peak in the pure ZrO_2 support (Biswas *et al.*, 2007). The key finding of Au deposition over both CeO_2 and ZrO_2 supports was to activate the hydrogen with subsequent spillover to the support and promote the support reduction peaks with lower reduction temperatures (Gamboa-Rosales *et al.*, 2012), as confirmed by the shifting of support reductions in all catalysts. This shifted was attributed to the strong interaction between metal and support due to the weakening of Ce–O bond by gold nanoparticles (Liu *et al.*, 2008). Therefore, the oxygen mobility was improved and facilitated the reduction of supports. The lowest reduction peaks at 96–147 °C were corresponded to the reduction of oxygen species adsorbed on Au_xO_y nanoparticles (Tabakova *et al.*, 2011). When focusing on the $Au/Ce_{0.75}Zr_{0.25}O_2$ catalyst, the reduction peak of $Au^{\delta+}$ species shifted to high temperature, indicating that the interaction between metal and metal was improved (Chang *et al.*, 2008). For the $Au/Ce_{0.5}Zr_{0.5}O_2$ and $Au/Ce_{0.25}Zr_{0.75}O_2$ catalysts, there were two main peaks of the Au reduction; the first peaks at 110 and 114 °C were attributed to the reduction of the Au^{3+} to Au^0, and the second peaks at 142–147 °C were assigned to the reduction of the Au^+ to Au^0 (Pojanavaraphan *et al.*, 2013). It was well–known that the area under the Au reduction peak could be related to the amount of $Au^{\delta+}$ species (Rynkowski *et al.*, 2009). It was found that the addition of $\geq$ 50 mol% Zr caused the decrease in peak area, indicating the increasing the amount of Au^0 content which was less reductive specie. The possible explanation was that the Au was hardly incorporated on the vacant Ce^{4+} sites, which promote the oxygen mobility, due to the shielding by zirconium (Dobrosz-Gómez *et al.*, 2009).

For the SN catalyst (Figure 4.6B), it showed three Au reduction peaks at 91, 129, and 158 °C, which associated with the Au^{3+} and Au^+ reductions, respectively. It could be seen that the CeO_2 reduction peak shifted to higher

temperature (456 °C), which correlated to the larger size of CeO_2 crystal structure due to the lack of solid solution phase.

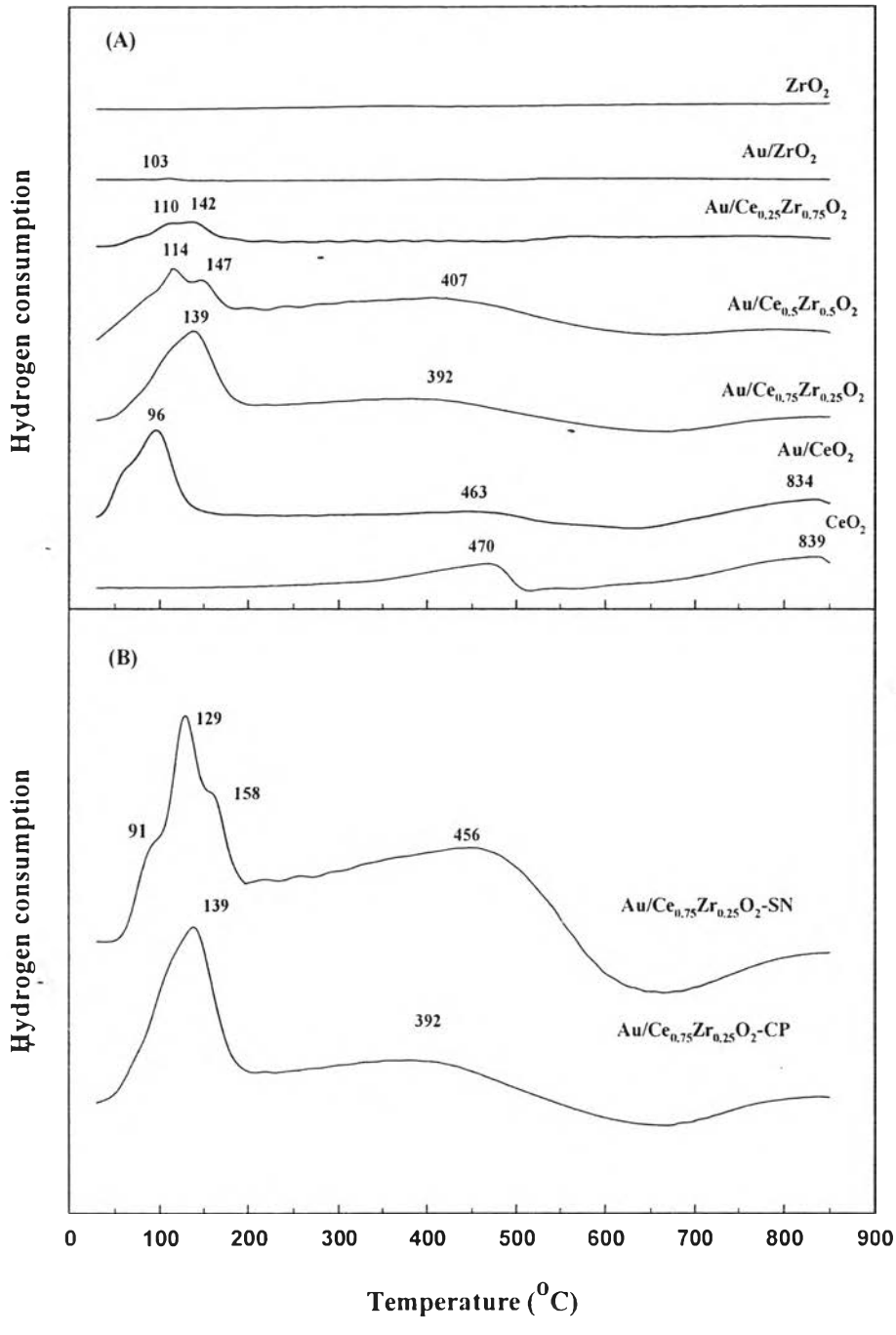

Figure 4.6 TPR profiles of 3 wt% $Au/CeO_2–ZrO_2$ calcined at 400 °C (A) Effect of support compositions. (B) Effect of support preparation techniques (CP: co–precipitaion, SN: sonochemical).

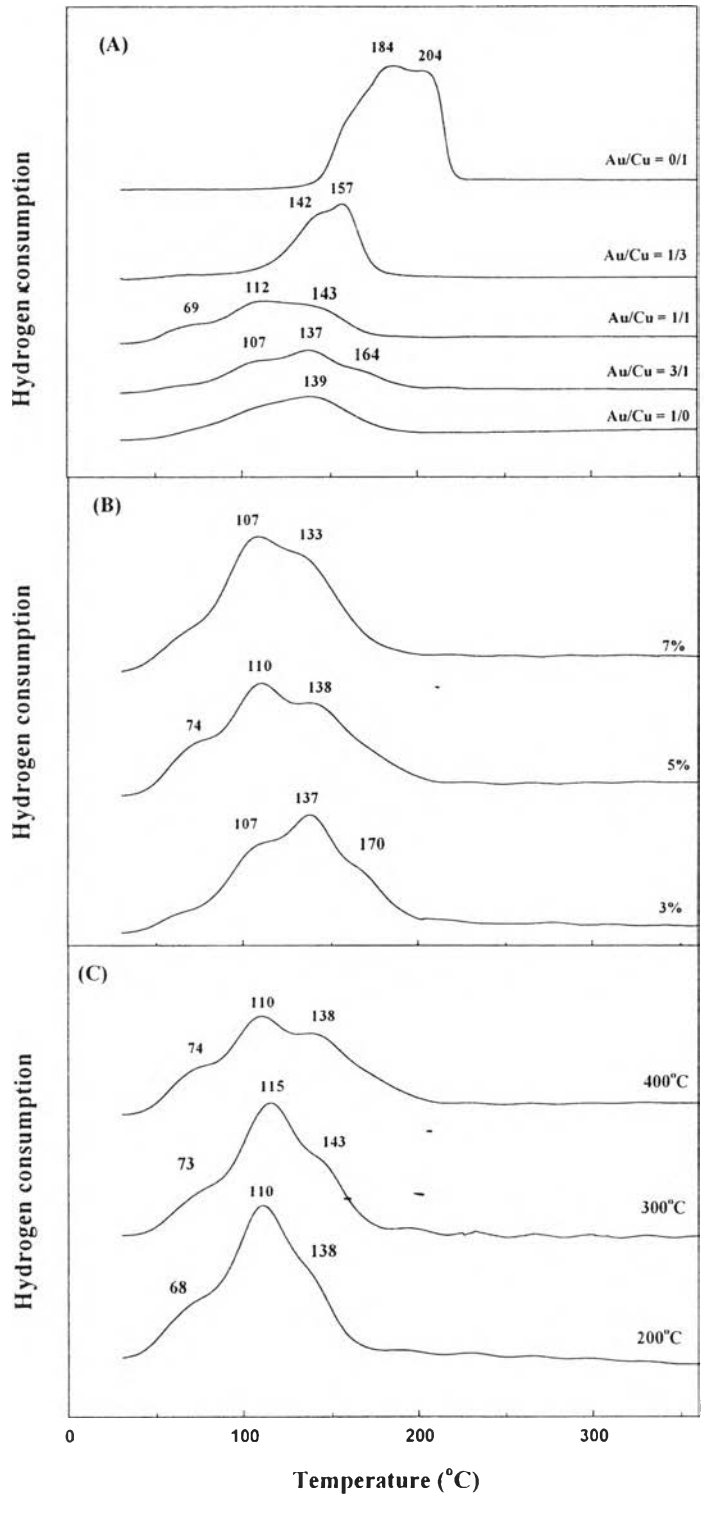

Figure 4.7 TPR profiles of Au–Cu/$CeO_{0.75}ZrO_{0.25}O_2$ catalysts (A) Effect of Au/Cu atomic ratios. (B) Effect of total metal loading. (C) Effect of calcination temperature.

The TPR profiles of bimetallic 3 wt% Au–Cu/$Ce_{0.75}Zr_{0.25}O_2$ catalysts with various Au/Cu atomic ratios were shown in Figure 4.7A. The reduction peaks of Cu/$Ce_{0.75}Zr_{0.25}O_2$ were observed at 184 °C and 204 °C, indicating two different kinds of copper oxide species. The low–temperature peak assigned to the small CuO particles which were highly dispersed and strongly interacted with the support (Agrell *et al.*, 2003), and the high–temperature peak represented larger size of CuO particles or the bulk CuO (Ratnasamy *et al.*, 2004). The reduction profiles of the bimetallic catalysts showed three main peaks, but their shifting behaviors depended on the Au/Cu atomic ratio. For instance, the lowest reduction temperature at 69 °C and 107 °C were corresponded to the Au reduction or reactive site of Au, whereas the second and the third peaks were attributed to partial merging between Au reduction and the highly dispersed CuO (Pojanavaraphan *et al.*, 2013), and the bulk CuO, respectively. When increasing the Cu contents from Au/Cu = 3/1 to 1/1, all reduction peaks shifted to lower temperatures since copper atoms affected on the electronic structure of gold by near–neighbor interactions (Chimentão *et al.*, 2007). In term of synergistic effect, Ou and coworkers, (2008) proposed that the lowering of reduction temperature was due to the enhancement of CuO dispersion by gold, which preserved smaller CuO particles. Moreover, gold in the catalyst could weaken the bond strength of Cu–O to improve the reducibility of CuO particles. This shifting could be correlated to the decreasing size of an alloy Au–Cu particle, which easily reduced at lower temperature (Llorca *et al.*, 2008). However, the copper–rich catalyst (Au/Cu=1/3) did not show the same trend because both low– and high– temperature peaks shifted to higher temperatures. The Au reduction peak had very small intensity, whereas other higher reduction peaks had much higher intensity and seemed to dominate. This may be due to the strength of Cu–O bond at high Cu content, resulting in the growth of alloy particles.

Figure 4.7B shows the TPR profiles of 3Au1Cu/$Ce_{0.75}Zr_{0.25}O_2$ catalysts with various total metal loadings. When increasing the total loading from 3 to 5 wt%, the reduction peaks were shifted to lower temperatures and the appearance of the low–temperature peak (<100 °C), which corresponded to the reactive site of gold species at the interface between the alloy and support, was also observed (Llorca *et al.*, 2008). This shifting in reduction temperature could be explained in

terms of size effect. Due to the favorable reduction of gold nanoparticles, the spillover of hydrogen was favored as the size of nanoparticle decreased. Therefore, the size of 5 wt% was smaller than 3 wt% catalysts. Focusing on the reduction profile of 7 wt% catalyst, the reduction peak at low–temperature did not observed, implying the decreasing of reactive sites of gold species.

When lowering the calcination temperature over the 5 wt% 3Au1Cu catalysts (Figure 4.7C), the reduction peak became symmetric and the intensities of all peaks also increased. The possible explanation was that the low intensity became from larger size of alloy particles which did not adsorb hydrogen to any appreciable extent (Chimentão *et al.*, 2007). Therefore, the catalyst calcined at 400 °C had the biggest size of alloy particle, whereas the smallest size was obtained from the catalyst calcined at 200 °C.

4.1.4 Atomic Absorption Spectroscopy (AAS)

Elemental analysis of catalysts was used to determine the metal composition of any catalysts (Table 4.1). For the monometallic Au catalysts, the maximum Au deposition was found in $Au/Ce_{0.75}Zr_{0.25}O_2$ catalyst with 2.88 wt%. After adding the Zr metal, the amount of actual Au deposited became decreasing was the consequence of the difference in electronic charge properties on the CeO_2–ZrO_2 surface, such as the point of zero charge (PZC). The PZC value of CeO_2 is ~7.27 and ZrO_2 is ~4.87 (Pojanavaraphan *et al.*, 2013). In our preparation procedures, the pH of solution was fixed at 8, hence, the difference value between the pH and PZC had an effect to the metal deposition. If the support had lower PZC value, the support was become more negative due to the removal of protons from the surface hydroxyls, resulting in the electrostatic repulsion of Au anions. Therefore, it could be confirmed the result which higher ZrO_2 content caused decreasing metal deposition in catalysts. Besides, Qian *et al.* (2010) reported that the Au particles preferred to interact with hydroxyl group on the oxide support surface, which could be provided by the support with high ceria content. Therefore, our results were in line with this report.

For the bimetallic Au–Cu catalysts, the results showed that the synthesized Au/Cu atomic ratio of 1/1 and 1/3 catalysts were closed to expected value, whereas, the ratio of 3/1 was higher than that of expected value. This may be

due to an error during the preparation step (Llorca *et al.*, 2008). In case of different total metal loadings, the catalyst with 5 wt% total metal loading had the Au/Cu atomic ratio about 3.02, which was closely to the expected value. Besides, the calcination temperature also affected on the deposition of metal content, as evidenced in Table 4.1. The highest amount of Au was deposited on the catalyst calcined at 300 °C. Moreover, it could be observed that as the calcination temperature increased, the Au/Cu atomic ratio also increased.

4.1.5 Fourier Transform Raman Spectra (FT-Raman)

Raman spectroscopy was used to investigate the catalyst modification for fresh and spent catalysts of $Au/Ce_{0.75}Zr_{0.25}O_2$ and $3Au1Cu/Ce_{0.75}Zr_{0.25}O_2$. The Raman spectras of $Au/Ce_{0.75}Zr_{0.25}O_2$ and $3Au1Cu/Ce_{0.75}Zr_{0.25}O_2$ were presented in Figure 4.8. The Raman spectra of $Au/Ce_{0.75}Zr_{0.25}O_2$ and $3Au1Cu/Ce_{0.75}Zr_{0.25}O_2$ catalysts consisted of two peaks at 463, 592 cm^{-1}, and 469, 561 cm^{-1}, respectively. The first peaks were attributed to the main Raman of CeO_2, which slightly shifted from the position that occupied in bulk at 464 cm^{-1} (Raman-active F_{2g} mode) (Gamboa-Rosales *et al.*, 2012). The explanation for this shift is that the frequency for the M–O vibration was changed after the incorporation with dopants (Katta *et al.*, 2010). Another peak was corresponded to wake Raman–active mode of CeO_2 or the presence of oxygen vacancies (O_v), which appeared on the structure of ceria as defects that promoted the tetragonalization of ceria by the presence of Ce^{3+} cations (Laguna *et al.*, 2014). These defects were called Frankel–type defects, which promoted the mobility of oxygen and enhanced redox properties of ceria as compared to ceria–zirconia (Mamontov *et al.*, 2000). It could be seen that the Raman peak which attributed to F_{2g} mode became prominent after exposure to the reaction. This may be due to the increasing of CeO_2 crystallite sizes (Bao *et al.*, 2008), as confirmed by XRD patterns (Figure 4.4A). Figure 4.8A presents the Raman spectra of $Au/Ce_{0.75}Zr_{0.25}O_2$. The result showed that the peak, which corresponded to the oxygen vacancies, was small. This was in accordance with Laguna and coworkers. They reported that the gold nanoparticles preferred to deposit on the oxygen vacancies in ceria that meant the existent interaction between gold and the oxygen vacancies in ceria (Laguna *et al.*, 2014). Focusing on $3Au1Cu/Ce_{0.75}Zr_{0.25}O_2$ catalyst,

as illustrated in Figure 4.8B, the Raman peak of fresh catalyst which attributed to the oxygen vacancies of ceria was increased as compared to pure gold catalyst. This may be due to the promotion of the oxygen vacancies by the inclusion of copper species. Furthermore, the Raman peak at 621 cm^{-1} which attributed to CuO was observed in this catalyst.

In order to estimate the concentration of oxygen vacancies on CeO_2–ZrO_2 mixed oxides catalysts, the intensity ratio between oxygen vacancies band and main Raman of CeO_2 band was calculated. Table 4.3 presents the Raman ratio for fresh and spent catalysts of $Au/Ce_{0.75}Zr_{0.25}O_2$ and $3Au1Cu/Ce_{0.75}Zr_{0.25}O_2$. The results showed that after exposure to the reaction, the Raman ratio decreased in all catalysts. The possible explanation was due to the adsorption of CO_2 on ceria surface that led to the decrease of the vacant sites for oxygen adsorption (Rajasree *et al.*, 2004). Hence, a number of oxygen vacancies were dropped because of the competition to adsorb between oxygen and CO_2 molecules.

Table 4.3 The intensity ratio of Raman bands of 3wt% $Au/Ce_{0.75}Zr_{0.25}O_2$ and $3Au1Cu/Ce_{0.75}Zr_{0.25}O_2$ catalysts

Catalysts	Calcination temperature (°C)	Raman ratio[a]
Fresh		
$Au/Ce_{0.75}Zr_{0.25}O_2$	400	3
$3Au1Cu/Ce_{0.75}Zr_{0.25}O_2$	400	7.11
Spent		
$Au/Ce_{0.75}Zr_{0.25}O_2$	400	0.27
$3Au1Cu/Ce_{0.75}Zr_{0.25}O_2$	400	0.01

[a] Calculated from the intensity ratio of Raman bands of I_{592}/I_{463} and I_{561}/I_{469} for $Au/Ce_{0.75}Zr_{0.25}O_2$ and $3Au1Cu/Ce_{0.75}Zr_{0.25}O_2$, respectively.

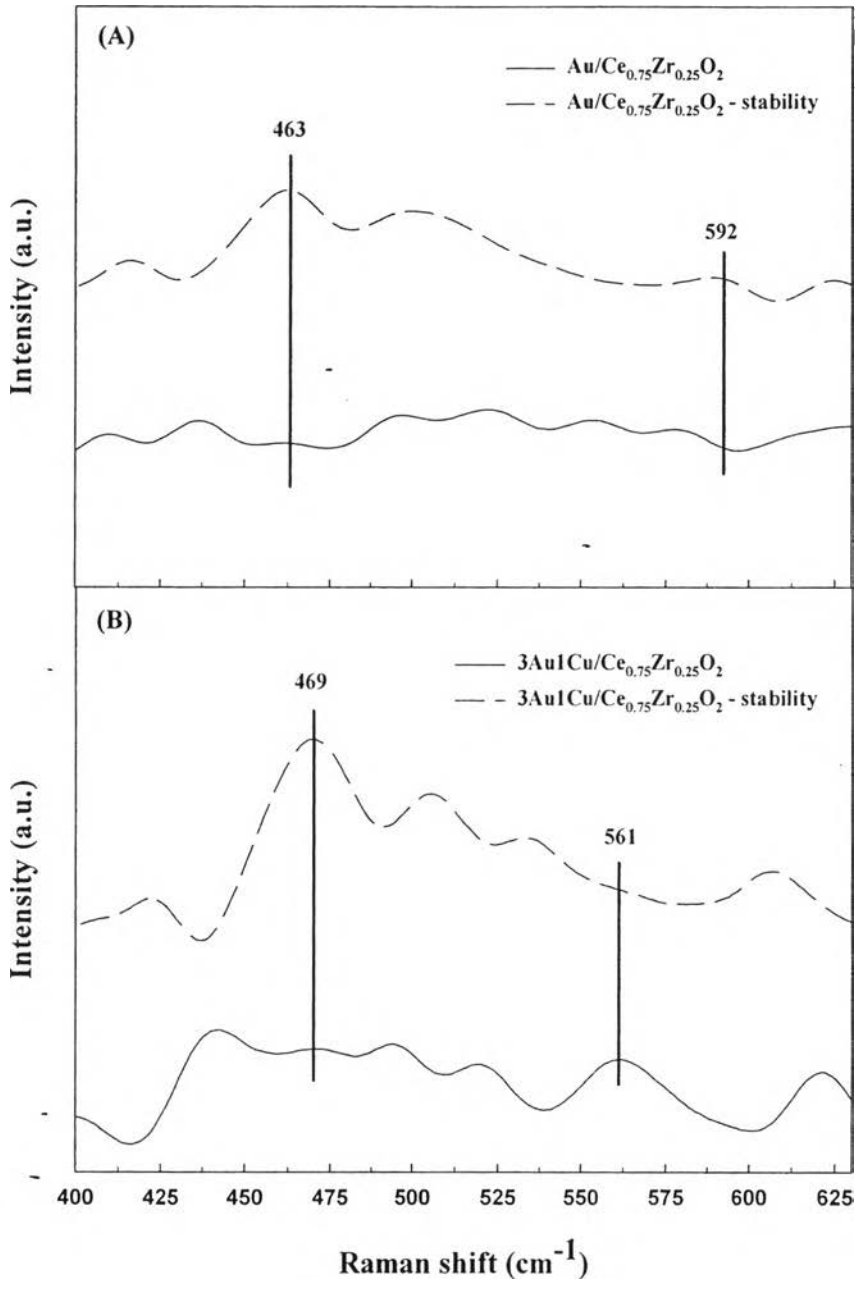

Figure 4.8 Raman spectra of fresh and spent catalysts (A) $Au/Ce_{0.75}Zr_{0.25}O_2$. (B) $3Au1Cu/Ce_{0.75}Zr_{0.25}O_2$.

4.1.6 Temperature-programmed Oxidation (TPO)

The temperature-programmed oxidation (TPO) technique was used to investigate a carbonaceous deposition (or coke) on the spent catalysts after exposure to the reaction at 350 °C for 21 h. Figure 4.9 shows the TPO profiles of 3 wt% $Au/Ce_{0.75}Zr_{0.25}O_2$ and 3 wt% $3Au1Cu/Ce_{0.75}Zr_{0.25}O_2$ catalysts. These two catalysts also exhibited the main peak around 224 °C, which corresponded to carbon–containing surface species (de Lima *et al.*, 2008). Moreover, the 3 wt% $3Au1Cu/Ce_{0.75}Zr_{0.25}O_2$ exhibited the peak at ~100 °C, which attributed to the decomposition of carbonates species (Yi *et al.*, 2010). The amount of coke was reported in Figure 4.9. Normally, the deactivation of catalysts occurred due to the carbon deposition which blocked the active sites and reduced the interaction of gas phase reaction on the surface (Halabi *et al.*, 2010). From the results, it could be seen that the 3 wt% $Au/Ce_{0.75}Zr_{0.25}O_2$ catalyst formed more coke than 3 wt% $3Au1Cu/Ce_{0.75}Zr_{0.25}O_2$ catalyst. This may be due to the activation of O_2 by copper. So, the coke was removed by an activated oxygen via coke gasification reaction (Pojanavaraphan *et al.*, 2013).

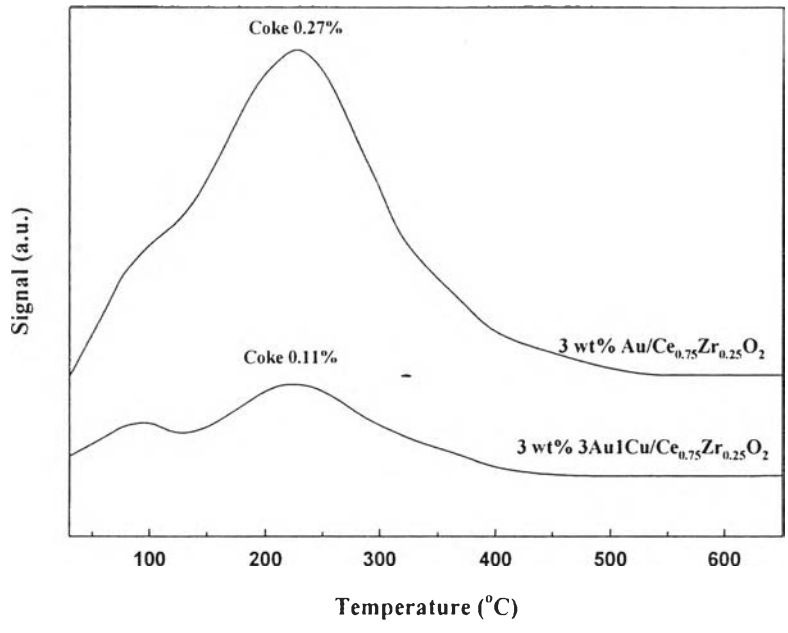

Figure 4.9 TPO profiles of 3 wt% $Au/Ce_{0.75}Zr_{0.25}O_2$ and 3 wt% 3Au1Cu/ $Ce_{0.75}Zr_{0.25}O_2$ catalysts after exposure to the reaction at 350 °C for 21 hours (Reaction conditions: $O_2/H_2O/CH_3OH$ molar ratio = 0.6:2:1).

4.1.7 UV-visible Spectroscopy

In order to identify the Au species, UV-spectroscopy was used. According to reference data, the band at 200–250 nm was attributed to the absorption of Au ions, the band between 280 and 380 nm was assigned to the partially charged $(Au)_n$ ($1<n<10$) clusters, and the band around 500–600 nm was corresponded to the absorptions of Au nanoparticles in metallic form (Sun *et al.*, 2010). Pure CeO_2 also exhibited the absorption band at 343–347 nm (Rao and Sahu, 2001). Besides, the absorption bands for mixed oxide, which were observed due to the defects of the ceria lattice inducing by Zr^{4+}, were reported by Kambolis *et al.* (2010). The absorption band of mixed oxide consisted of 2 areas; first, 313–317 nm, which was attributed to $Ce^{4+} \leftarrow O^{2-}$, and another band at 235–240 nm, which was ascribed to $Ce^{3+} \leftarrow O^{2-}$ and/or $Zr^{4+} \leftarrow O^{2-}$ charge transfer. The fact that the bands were composed of multiple peaks could be explained by the diversity of the cations environment and the two oxidation states of cerium (Kambolis *et al.*, 2010). Figure 4.10 shows the UV-vis spectra of 3 wt% $Au/CeO_2–ZrO_2$ catalysts with different

support compositions. It could be observed that the small absorption band of Au metallic species was found on $Au/Ce_{0.75}Zr_{0.25}O_2$, $Au/Ce_{0.5}Zr_{0.5}O_2$, and $Au/Ce_{0.25}Zr_{0.75}O_2$ catalysts. The small band of the Au clusters (~287 nm) was detected in $Au/Ce_{0.75}Zr_{0.25}O_2$ and $Au/Ce_{0.5}Zr_{0.5}O_2$ catalysts. However, the Au cationic species was hardly to identify due to the overlap between Au cationic species and the mixed oxide support.

When comparing the absorption bands between the CP and SN catalysts (Figure 4.11), the result indicated that the SN catalyst exhibited a tiny band of Au clusters. However, no Au metallic and Au cationic species were observed. This may be due to the decreasing of gold particle size which originated from an ultrasonic pretreatment. Therefore, the morphology of the support and the interaction between metal and support were changed (Tu *et al.*, 2009). This result reinforced similar conclusions for XRD and TPR results.

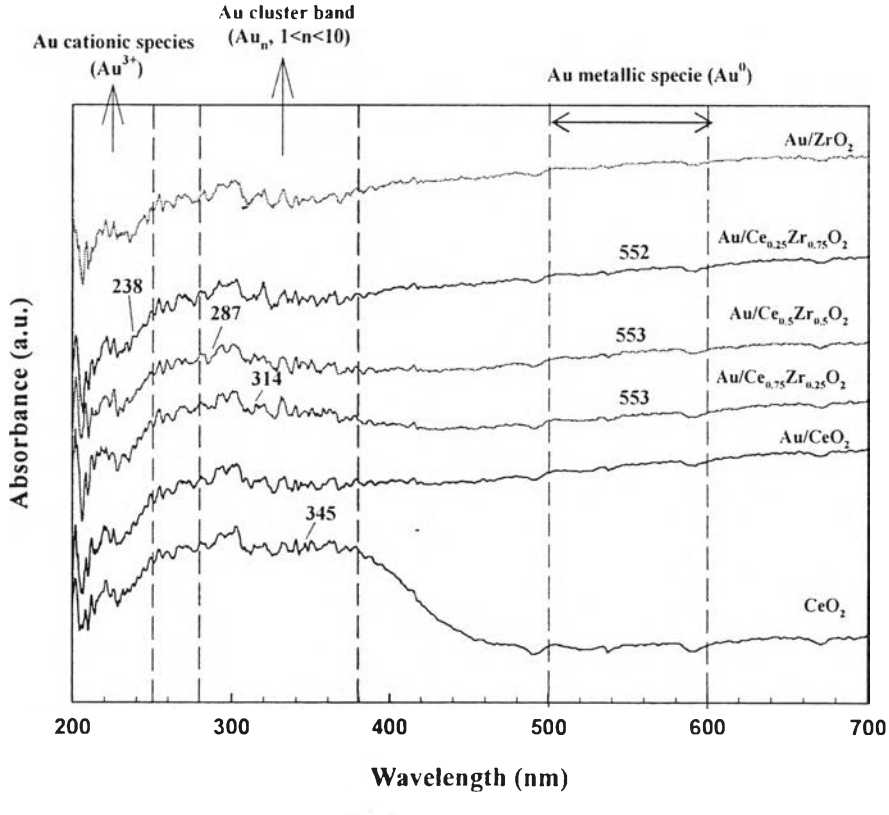

Figure 4.10 Diffuse reflectance UV-vis spectra of the Au species on 3 wt% Au/CeO_2–ZrO_2 catalysts calcined at 400 °C with different support compositions.

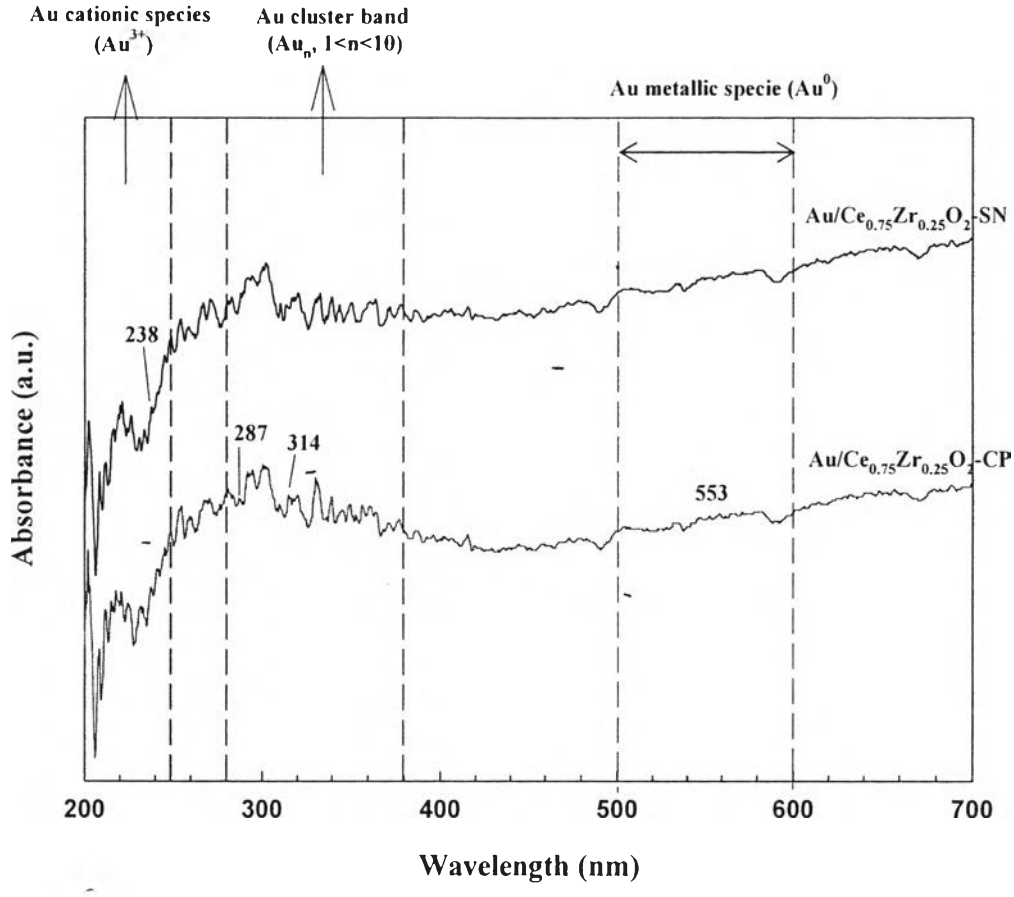

Figure 4.11 Diffuse reflectance UV-vis spectra of the Au species with various support preparation techniques over 3 wt% $Au/Ce_{0.75}Zr_{0.25}O_2$ catalysts calcined at 400 °C.

Figure 4.12 showed UV-vis spectra of 3 wt% $Au–Cu/Ce_{0.75}Zr_{0.25}O_2$ catalyst with various Au/Cu atomic ratios. It could be seen that the Au metallic specie was detected in Au/Cu atomic ratio of 1/0 and 1/3 of $Au–Cu/Ce_{0.75}Zr_{0.25}O_2$ catalysts. The absorption bands of Au cluster and $Cu^{2+} \leftarrow O^{2-}$ charge transfer (~265 nm) did not observed in all bimetallic catalysts (Mozer *et al.*, 2009). However, the absorption band of surface plasmon resonance of metallic copper at ~580 nm was detected in all bimetallic and pure Cu catalysts. Therefore, the results implied that Cu might be composed of metallic copper in the monometallic and bimetallic sample (Sandoval *et al.*, 2013).

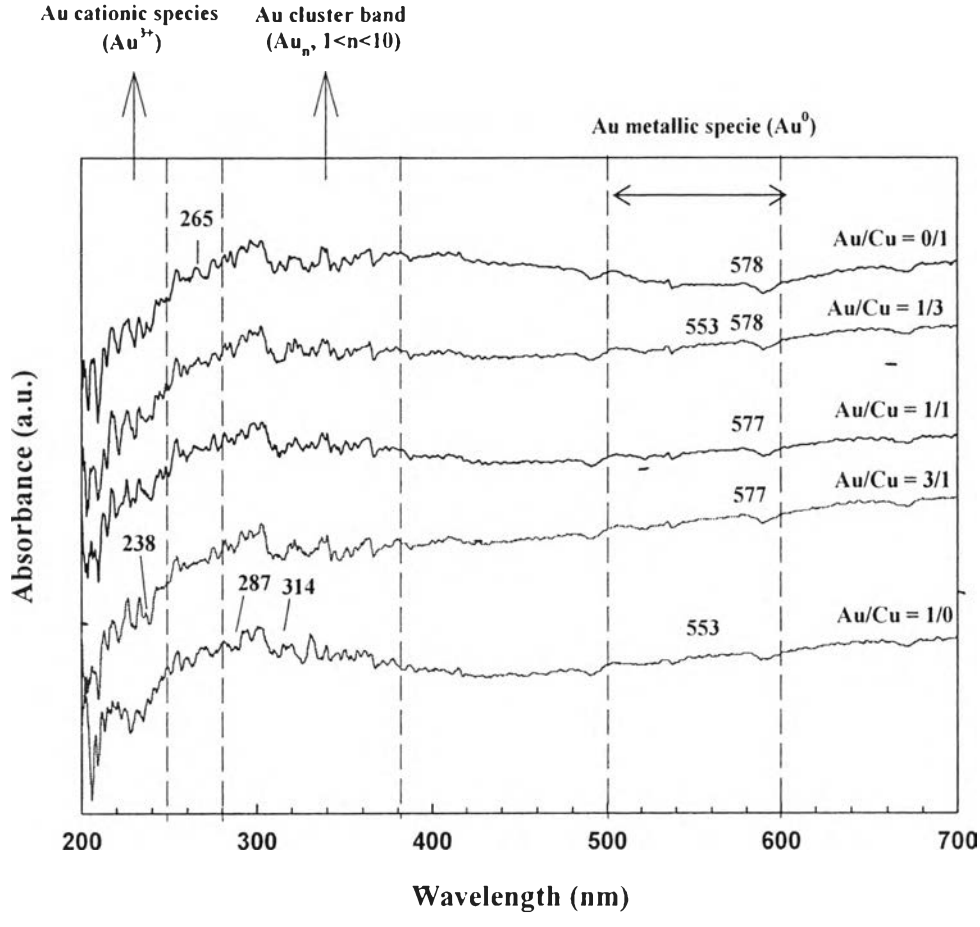

Figure 4.12 Diffuse reflectance UV-vis spectra of the Au species on 3 wt% Au–Cu/ $Ce_{0.75}Zr_{0.25}O_2$ catalyst calcined at 400 °C with different Au/Cu atomic ratios.

The UV-vis spectra of bimetallic 3Au1Cu/$Ce_{0.75}Zr_{0.25}O_2$ catalysts with various total metal loading was shown in Figure 4.13(A). The result showed that only metallic copper specie was founded at ~580 nm in all bimetallic catalysts. Besides, the absorption band around 318 nm, which attributed to $Ce^{4+} \leftarrow O^{2-}$, slightly shifted from 314 nm due to the band reflecting defects (Kambolis *et al.*, 2010). When varying the calcination temperature, it could be seen that the absorption band of Cu metallic specie was observed in all samples, whereas no absorption band of Au metallic specie was found. Furthermore, the band of Cu metallic specie was obviously seen, when the calcination temperature increased from 200 to 400 °C, as confirmed by Figure 4.13(B).

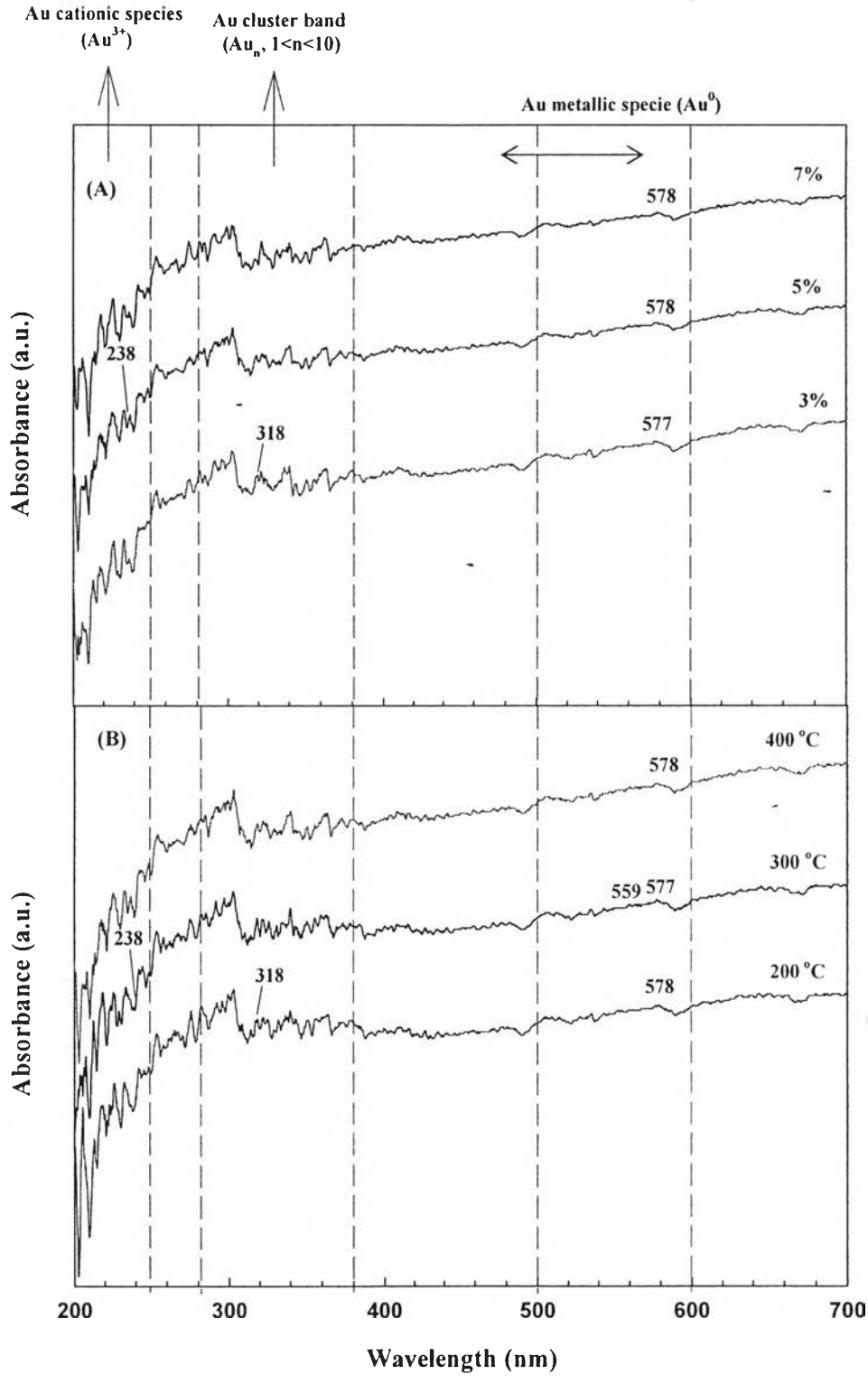

Figure 4.13 Diffuse reflectance UV-vis spectra of the Au species on 3Au1Cu/ $Ce_{0.75}Zr_{0.25}O_2$ catalyst (A) Effect of total metal loading. (B) Effect of calcination temperature.

4.2 Evaluation of Catalytic Activity

In this part, the catalytic activity of catalysts was tested in the oxidative steam reforming of methanol (OSRM) reaction by using the catalysts which prepared by several techniques such as the pure supports (CeO_2 and ZrO_2) were prepared by precipitation technique, the mixed supports (CeO_2–ZrO_2) were prepared by co–precipitation (CP) and sonochemical techniques, the monometallic catalysts and bimetallic catalysts were prepared by deposition–precipitation (DP), deposition–coprecipitation (DCP), and deposition–sonochemical techniques. Several effects were studied in detail such as effect of support composition (Ce/Ce+Zr atomic ratio), support preparation, Au/Cu atomic ratio, total metal loading, calcination temperature, and side reactions.

The catalytic activity tests were carried out in a vertical pyrex glass microreactor by packing 100 mg of 80-120 mesh catalyst inside. The activity was investigated at the temperature in range of 200 to 400 °C under an atmospheric pressure with $O_2/H_2O/CH_3OH$ molar ratio of 0.6/2/1.

4.2.1 Effect of Support composition on the Catalytic Performance

To study the effect of support composition on the catalytic performance of 3 wt% Au/CeO_2–ZrO_2 catalysts, the atomic ratios of Ce/(Ce+Zr) were varied from 0, 0.25, 0.5, 0.75, and 1. All of catalysts were calcined at 400 °C for 4 hours. Figure 4.14 showed the methanol conversion and hydrogen yield of supported Au catalysts with different support compositions (Ce/(Ce+Zr) atomic ratio). The highest catalytic activity was obtained by 3 wt% Au/$Ce_{0.75}Zr_{0.25}O_2$ catalysts with methanol conversion 96.68% and hydrogen yield 59.72% at 400 °C. In term of gas product selectivity, it was found that the CO_2 concentration in all catalysts decreased as the temperature increased whereas the CO concentration increased. The explanation was that CO could be formed by methanol decomposition (MD) reaction. Moreover, methane also formed during OSRM reaction and it was observed on the 3 wt% Au/$Ce_{0.25}Zr_{0.75}O_2$ and 3 wt% Au/ZrO_2 catalysts because ZrO_2 promoted side reactions (Decarbonylation of acetaldehyde: $CH_3CHO \rightarrow CO + CH_4$) (Bi *et al.*, 2007). From figures 4.14 and 4.15, the 3 wt% Au/$Ce_{0.75}Zr_{0.25}O_2$ showed

the highest activity. This was in agreement with Biswas and coworker (2007). They explained that it may be due to the high oxygen storage capacity of $Ce_{0.75}Zr_{0.25}O_2$ that helped to increase the availability of surface oxygen and enhanced the WGS reaction (Biswas *et al.*, 2007). Besides this explanation, the amount of metal content also related to the catalytic activity because metal acted as the active species to stimulate the reaction. Table 4.1 showed the chemical composition of gold–based catalysts. It could be noticed that the $Au/Ce_{0.75}Zr_{0.25}O_2$ catalyst had the highest amount of gold content. Nevertheless, the surface area of catalysts, as shown in Table 4.1, did not affect to the catalytic activity for OSRM reaction. From the results, it could be reported that support composition played an important role to the catalytic activity on OSRM reaction and the Au catalyst supported on $Ce_{0.75}Zr_{0.25}O_2$ gave the highest activity. So, the 3 wt% $Au/Ce_{0.75}Zr_{0.25}O_2$ was chosen for further study.

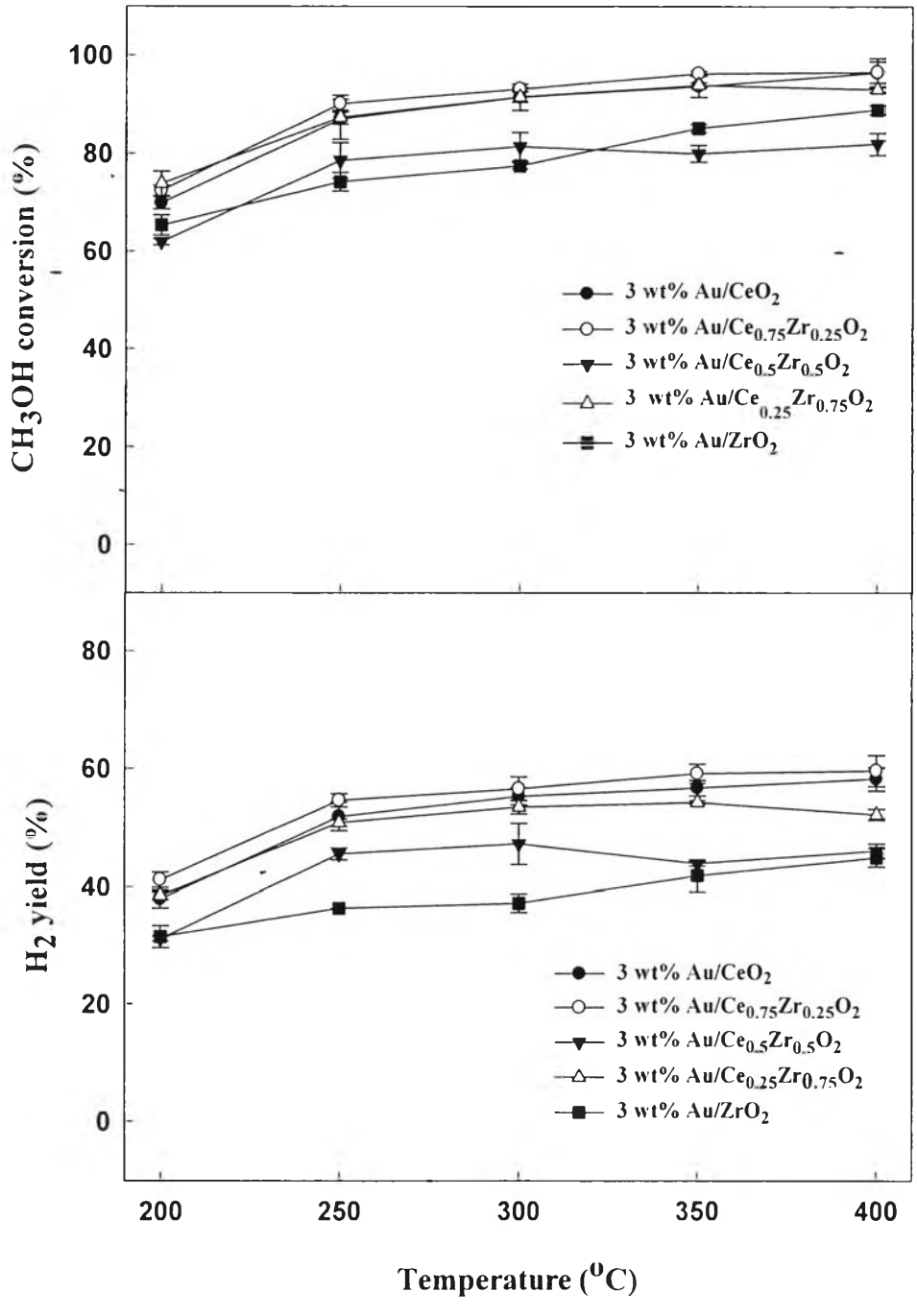

Figure 4.14 Effect of support composition on the methanol conversion and hydrogen yield over 3 wt% of Au/CeO_2–ZrO_2 catalysts calcined at 400 °C (Reaction condition: $O_2/H_2O/CH_3OH$ molar ratio = 0.6:2:1).

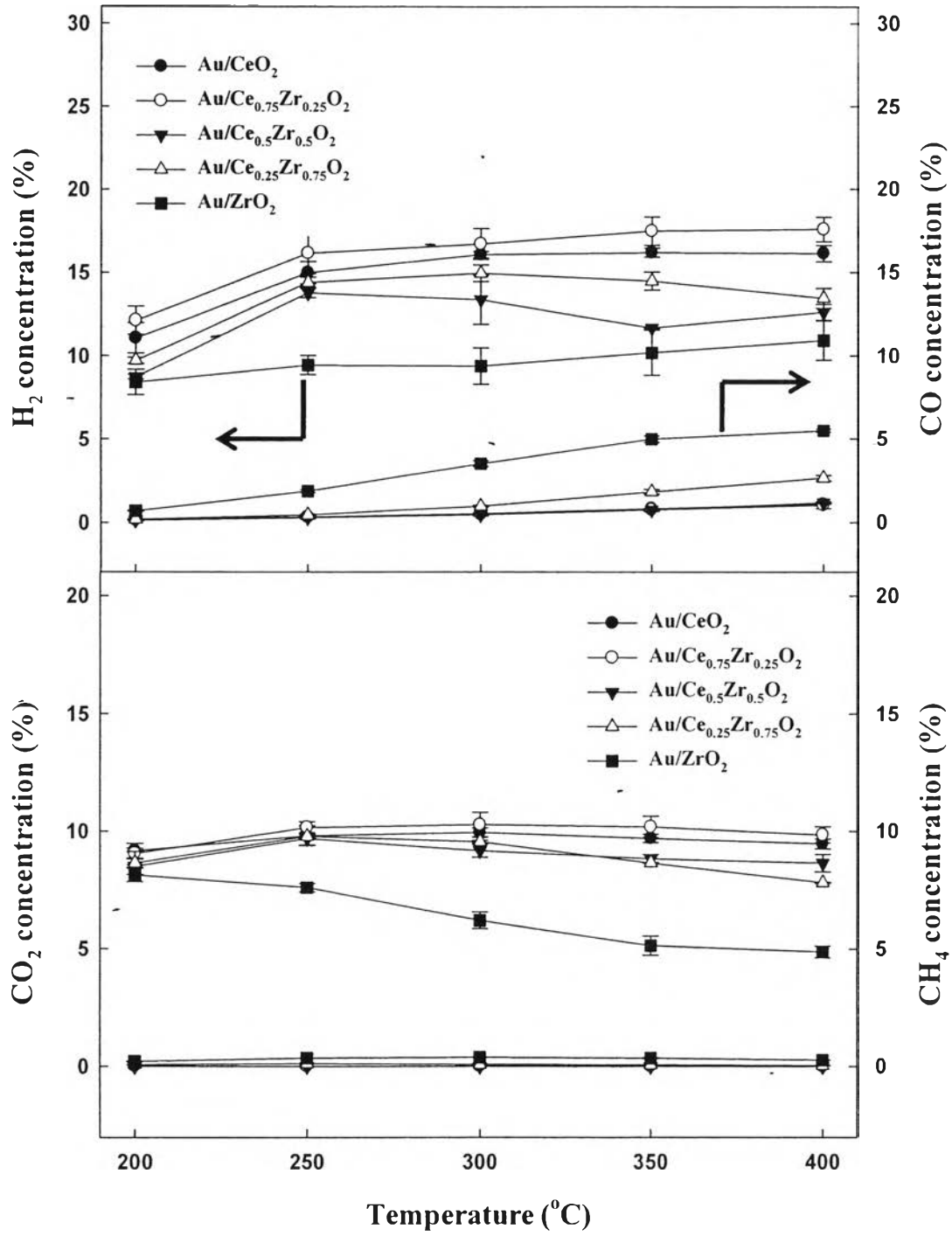

Figure 4.15 Effect of support composition on the concentration of H_2, CO, CO_2, and CH_4 over 3 wt% of $Au/CeO_2–ZrO_2$ catalysts calcined at 400 °C (Reaction conditions: $O_2/H_2O/CH_3OH$ molar ratio = 0.6:2:1).

4.2.2 Effect of Support Preparation on the Catalytic Performance

To study the effect of support preparation on the catalytic performance of 3 wt% Au/$Ce_{0.75}Zr_{0.25}O_2$ catalyst, the $Ce_{0.75}Zr_{0.25}O_2$ support was prepared by using 2 techniques; co–precipitation (CP), and sonochemical (SN). These supports were calcined at 400 °C for 4 hours. The 3 wt% Au was loaded on the supports by deposition-precipitation technique.

It could be seen that both methanol conversion and hydrogen yield increased in all of the reaction temperature range. The highest catalytic activity was observed on the 3 wt% Au/$Ce_{0.75}Zr_{0.25}O_2$ catalyst, which prepared by co–precipitation technique, as shown in Figure 4.16. The methanol conversion and hydrogen yield of 3 wt% Au/$Ce_{0.75}Zr_{0.25}O_2$–CP equaled to 96.68% and 59.72%, respectively. Figure 4.17 shows the concentration of H_2, CO, and CO_2 in catalysts. It can be reported that the concentration of H_2, CO, and CO_2 of these catalysts slightly different. However, no methane was observed on this testing. This result can be related to the Au deposition, as evidenced in Table 4.1. Due to the CP catalyst had the amount of gold deposition higher than SN catalyst. The CP catalyst may provide the catalytic activity, as compared to SN catalyst. Besides the metal content, the crystallite size of ceria also affected to the catalytic activity of catalyst on OSRM reaction. Because of the ceria crystallite growth of prepared catalyst via sonochemical technique, the formation of solid solution was less stable than co–precipitation technique, which caused the inconvenience to provide the oxygen mobility (Katta *et al.*, 2010). So, the $Ce_{0.75}Zr_{0.25}O_2$ support prepared by co–precipitation technique was chosen for further study.

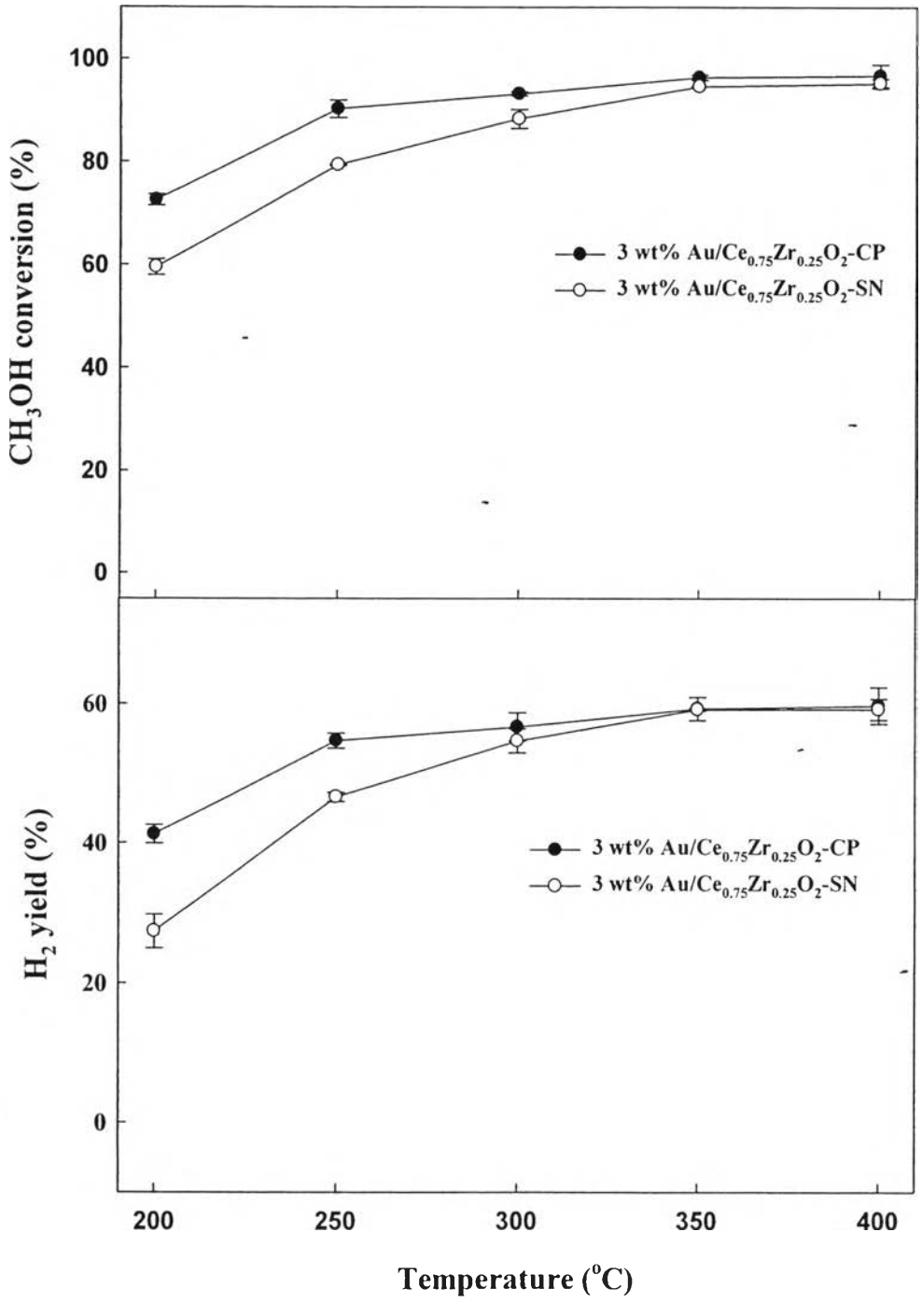

Figure 4.16 Effect of support preparation on methanol conversion and hydrogen yield over 3 wt% $Au/Ce_{0.75}Zr_{0.2}5O_2$ catalysts with co–precipitation (CP), and sonochemical (SN) techniques (Reaction conditions: O_2/ H_2O/CH_3OH molar ratio = 0.6:2:1).

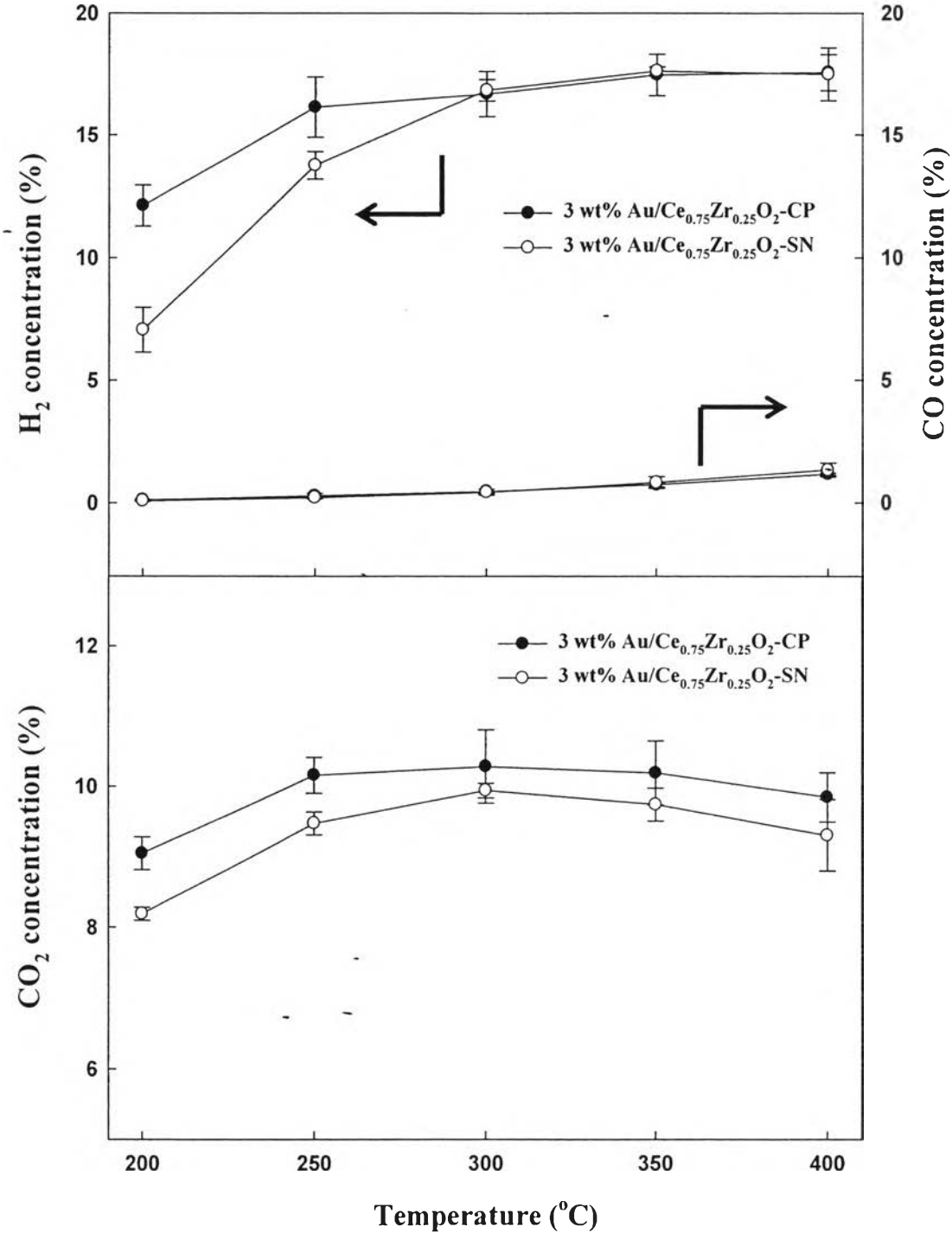

Figure 4.17 Effect of support preparation on the concentration of H_2, CO, CO_2 over 3 wt% $Au/Ce_{0.75}Zr_{0.25}O_2$ catalysts with co–precipitation (CP), and sonochemical (SN) techniques (Reaction conditions: O_2/ H_2O/CH_3OH molar ratio = 0.6:2:1).

4.2.3 Effect of Au/Cu Atomic Ratio

The influence of Au/Cu atomic ratios on bimetallic Au–Cu/$Ce_{0.75}Zr_{0.25}O_2$ catalysts with a fixed total metal loading of 3 wt% was studied by varying Au/Cu atomic ratio (1/0, 3/1, 1/1, 1/3, and 0/1). The $Ce_{0.75}Zr_{0.25}O_2$ support was prepared by co-precipitation technique, after that the metals (Au or Cu) were loaded on the support by deposition–precipitation technique. All of catalysts were calcined at 400°C for 4 hours, and tested the catalytic activity at the reaction condition of $O_2/H_2O/CH_3OH$ molar ratio = 0.6:2:1.

Figure 4.18 shows the methanol conversion and H_2 yield of Au–Cu/$Ce_{0.75}Zr_{0.25}O_2$ with 3 wt% total metal loading. The results showed that Au/$Ce_{0.75}Zr_{0.25}O_2$ and Cu/$Ce_{0.75}Zr_{0.25}O_2$ catalysts exhibited the catalytic activity higher than the bimetallic Au–Cu/$Ce_{0.75}Zr_{0.25}O_2$ catalysts. Nevertheless, the bimetallic catalyst with Au/Cu atomic ratio of 3/1 gave the highest catalytic activity as compared to 1/1, and 1/3. The possible explanation was that higher Au/Cu atomic ratios stimulated the weakly adsorbed species (molecular oxygen, other key species related with oxygen activation) to quickly desorb. Copper species played an important role in activating oxygen molecules that brought it to react with CO (Liu *et al.*, 2011). Moreover, Liu *et al.* (2011) founded that even a little amount of copper could control the agglomeration of gold, as confirmed by XRD result (Figure 4.2). Liao *et al.* (2013) found that the factors which related to the catalytic activity of catalysts were structure and surface compositions of Au–Cu bimetallic catalysts. From this result, it can be concluded that the bimetallic catalysts did not enhance the catalytic activity of catalysts on OSRM reaction much. However, many literatures reported that the introduction of copper can be helped to stabilize the catalytic activity of gold catalysts during the reaction (Li *et al.*, 2012).

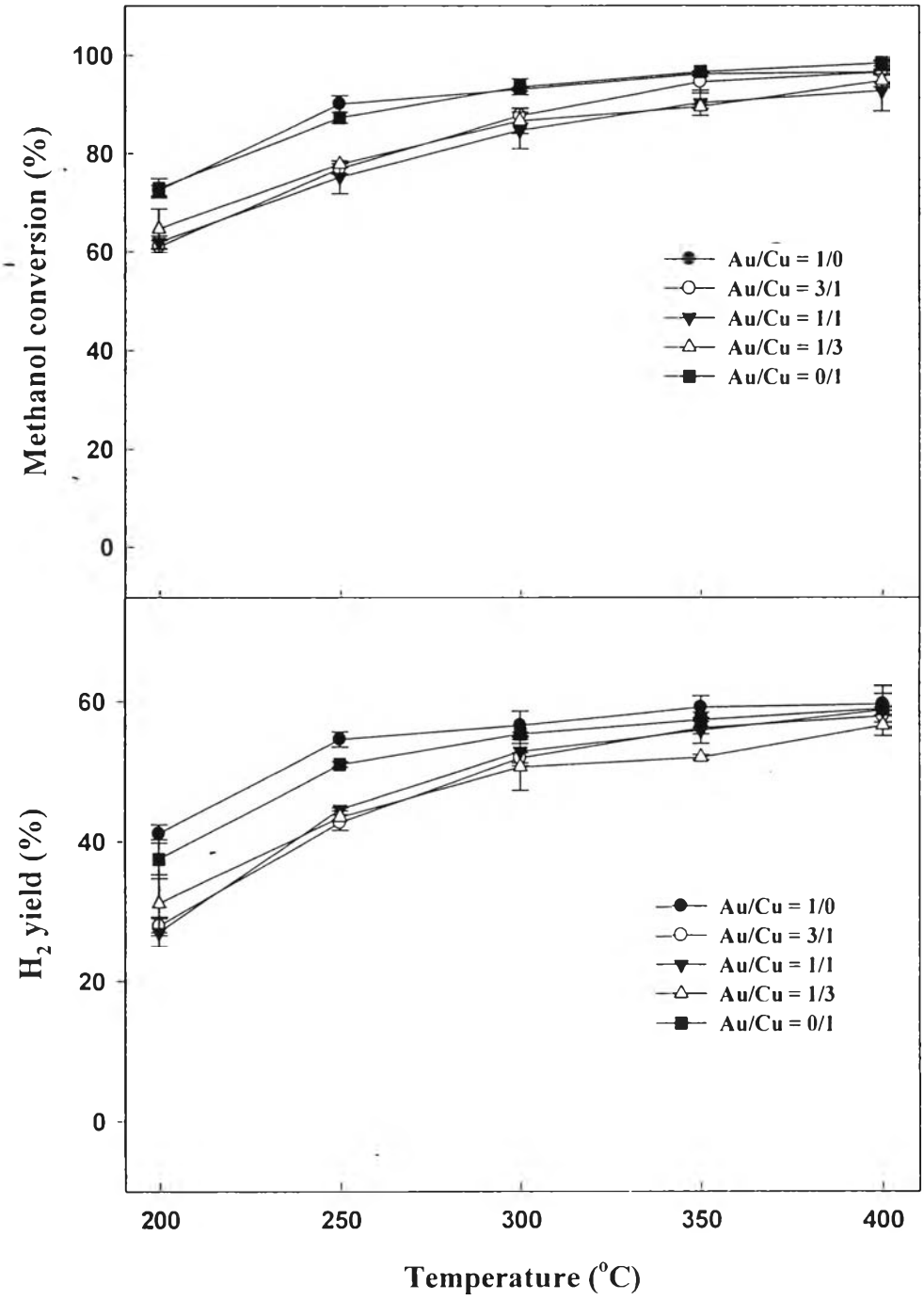

Figure 4.18 Effect of Au/Cu atomic ratio on the methanol conversion and hydrogen yield over 3 wt% Au–Cu/$Ce_{0.75}Zr_{0.25}O_2$ catalysts calcined at 400 °C (Reaction conditions: $O_2/H_2O/CH_3OH$ molar ratio = 0.6:2:1).

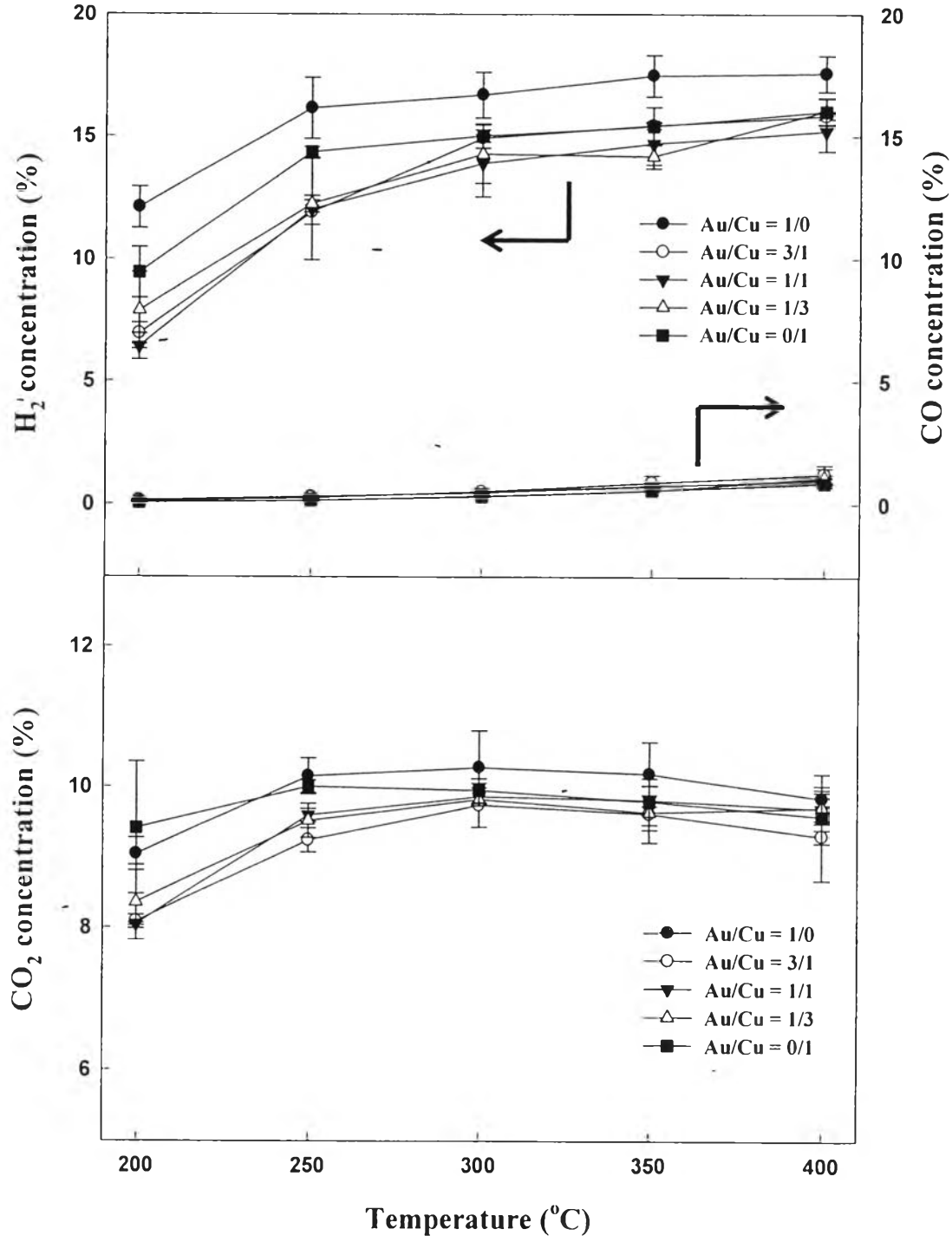

Figure 4.19 Effect of Au/Cu atomic ratio on the concentration of H_2, CO, and CO_2 over 3 wt% Au–Cu/$Ce_{0.75}Zr_{0.25}O_2$ catalysts calcined at 400 °C (Reaction conditions: $O_2/H_2O/CH_3OH$ molar ratio = 0.6:2:1).

4.2.4 Effect of Stability between $Au/Ce_{0.75}Zr_{0.25}O_2$, $Au-Cu/Ce_{0.75}Zr_{0.25}O_2$, and $Cu/Ce_{0.75}Zr_{0.25}O_2$ catalysts with 3% total metal loading

The stability of $Au/Ce_{0.75}Zr_{0.25}O_2$, $Au–Cu/Ce_{0.75}Zr_{0.25}O_2$, and $Cu/Ce_{0.75}Zr_{0.25}O_2$ catalysts were tested for 21 hours (1260 minutes) at 350°C, as shown in Figure 4.20. The activity of catalyst, which had Au/Cu atomic ratio of 3/1, showed stable catalytic activity over the whole reaction testing, as compared to other ratios. The methanol conversion was slightly increased from 94.62% to 94.79% and hydrogen yield from 56.18% to 57.20%, whereas the $Au–Cu/Ce_{0.75}Zr_{0.25}O_2$ catalysts which had Au/Cu atomic ratio of 1/1 and 1/3 slightly dropped. The possible explanation was that the arising of the electronic effect, which brought by copper, was happened (Liu *et al.*, 2011). Besides, this may be due to the addition of water and oxygen which helped to clean the metal surface and kept it active for a long time. The water vapor had a significant positive effect due to the following reasons, (i) improvement of the WGS reaction, (ii) hydroxyl groups formed by dissociative adsorption of H_2O on gold were generated the active sites, and (iii) promotion of the decomposition of carbonate species (Liao *et al.*, 2013). Moreover, the presence of steam or water can reduce the risk of coke formation due to the providing of oxygen for cleaning mechanism by Type II bridging OH groups (da Silva *et al.*, 2011). In the presence of oxygen, the vacancies of support can be replenished. Therefore, the bimetallic catalyst which had Au/Cu atomic ratio of 3/1 was chosen for comparing to $Au/Ce_{0.75}Zr_{0.25}O_2$ and $Cu/Ce_{0.75}Zr_{0.25}O_2$ catalysts. From this testing, the methanol conversions of $Au/Ce_{0.75}Zr_{0.25}O_2$, and $Cu/Ce_{0.75}Zr_{0.25}O_2$ were dropped from 96.50% to 90.16% and 96.02% to 91.81%, respectively. The result was in accordance with Pasini *et al.* (2011). They founded that the bimetallic Au–Cu catalysts exhibited stable catalytic performance. The dropped of catalytic activity may be due to the agglomeration of Au nanoparticles, as confirmed by Table 4.2. It can be seen that the average crystallite size of Au nanoparticles on $Au/Ce_{0.75}Zr_{0.25}O_2$ catalyst increased from 3.53 to 8.37 nm. Moreover, the possible reason for the dropped of catalytic activity was the decreasing of the raman ratio, which correlated to the amount of an oxygen vacancy (Bao *et al.*, 2008), as shown in Table 4.3. However, the raman ratio of the bimetallic also decreased, but the activity of this catalyst did not drop. This may be due to the enhancement of activity and stability arising from Au and Cu

interaction. The Au–Cu interaction caused by the redox properties of Cu, which stabilized the active gold species and prevented the gold particle growth (Ou *et al.*, 2008). From the results, it indicated that the bimetallic catalyst which had Au/Cu atomic ratio equal to 3/1 exhibited high catalytic performance over the other catalysts. So, the supported catalyst, which had Au/Cu atomic ratio of 3/1 was chosen for further study.

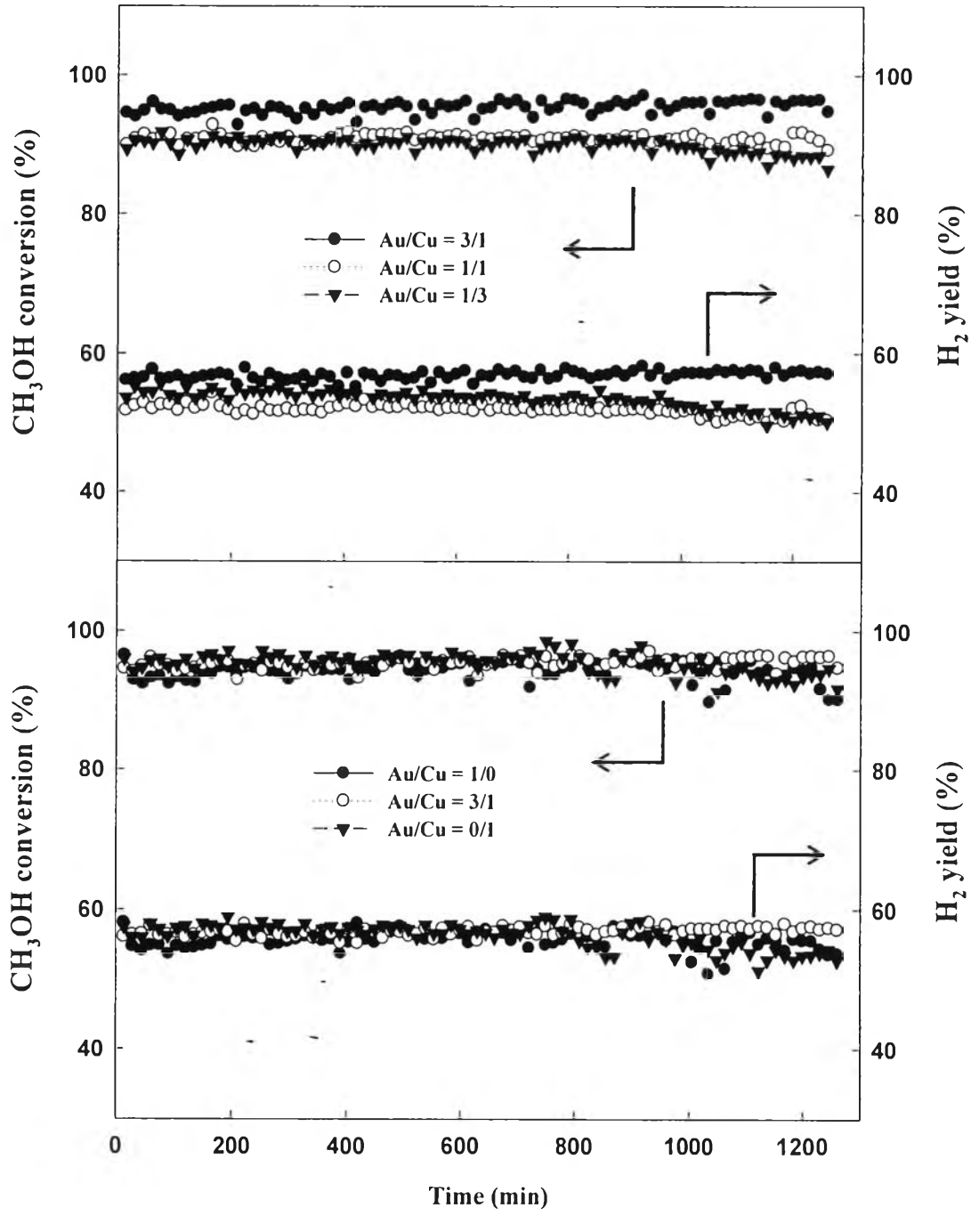

Figure 4.20 Stability testing of the $Au/Ce_{0.75}Zr_{0.25}O_2$, $Au–Cu/Ce_{0.75}Zr_{0.25}O_2$, and $Cu/Ce_{0.75}Zr_{0.25}O_2$ catalysts at 350 °C for 21 hours (Reaction conditions: $O_2/H_2O/CH_3OH$ molar ratio = 0.6:2:1).

4.2.5 Effect of Total Metal Loading on the Catalytic Performance

The effect of total metal loading on 3Au1Cu/$Ce_{0.75}Zr_{0.25}O_2$ catalysts was studied by varying the metal content (3, 5, and 7 wt%). The $Ce_{0.75}Zr_{025}O_2$ support was prepared by co–precipitation technique, after that the metals (Au and Cu) were loaded on the support by deposition–precipitation technique. All of catalysts were calcined at 400 °C for 4 hours.

The methanol conversion and hydrogen yield of 3Au1Cu/$Ce_{0.75}Zr_{0.25}O_2$ catalysts with various total metal loadings were shown in Figure 4.21. With an increase in total metal loading, the methanol conversion also increased and nearly completed conversion in 5 wt% and 7 wt% catalysts. The variation of the selectivity of H_2, CO, and CO_2 was shown in Figure 4.22. It was found that the activity of 5 wt% and 7 wt% catalysts was comparable. The possible explanation was the balancing between Au cationic and Au metallic species in 5 wt% catalyst, as confirmed by UV-vis spectra in Figure 4.13(A). Fierro-Gonzalez *et al.* (2007) reported that CO oxidation was active by the presence of metallic gold and cationic gold specie together due to the preferable adsorption of CO on metallic gold and cationic gold species. Besides, Au–O–Ce structure was responsible for WGS reaction (Deng *et al.*, 2005). Moreover, the performance of 5 wt% catalyst may be correlated to several factors; (i) the dispersion of Au specie on the support surface (ii) surface exposure of the Au cationic species, and (iii) a synergetic effect between the gold nanoparticles and the CeO_2 nanoparticle size, as confirmed by XRD and UV-vis spectra (Escamilla-Perea *et al.*, 2010). Therefore, the 5 wt% catalyst was chosen for further study.

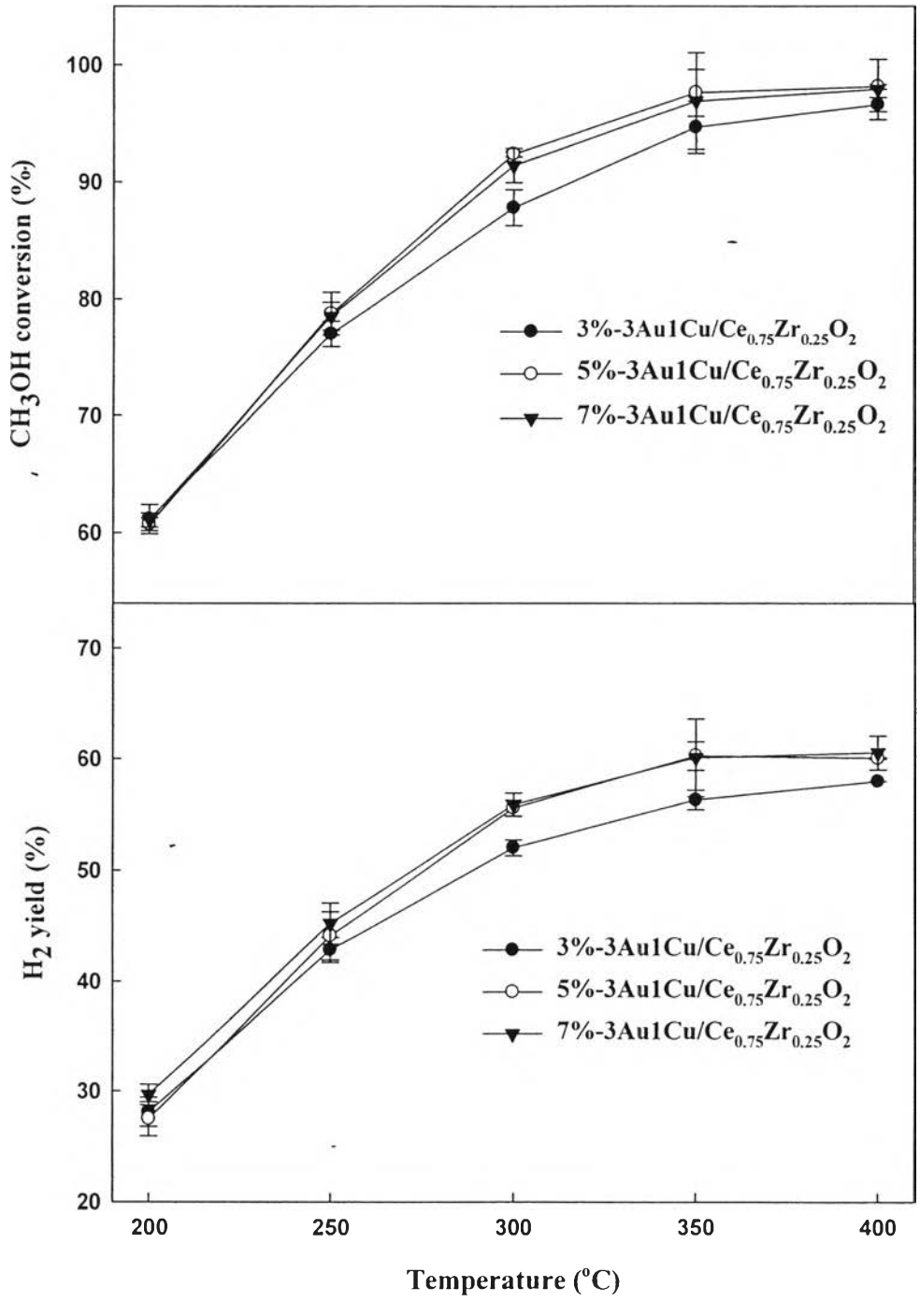

Figure 4.21 Effect of total metal loading on the methanol conversion and hydrogen yield over $3Au1Cu/Ce_{0.75}Zr_{0.25}O_2$ catalysts calcined at 400 °C (Reaction conditions: $O_2/H_2O/CH_3OH$ molar ratio = 0.6:2:1).

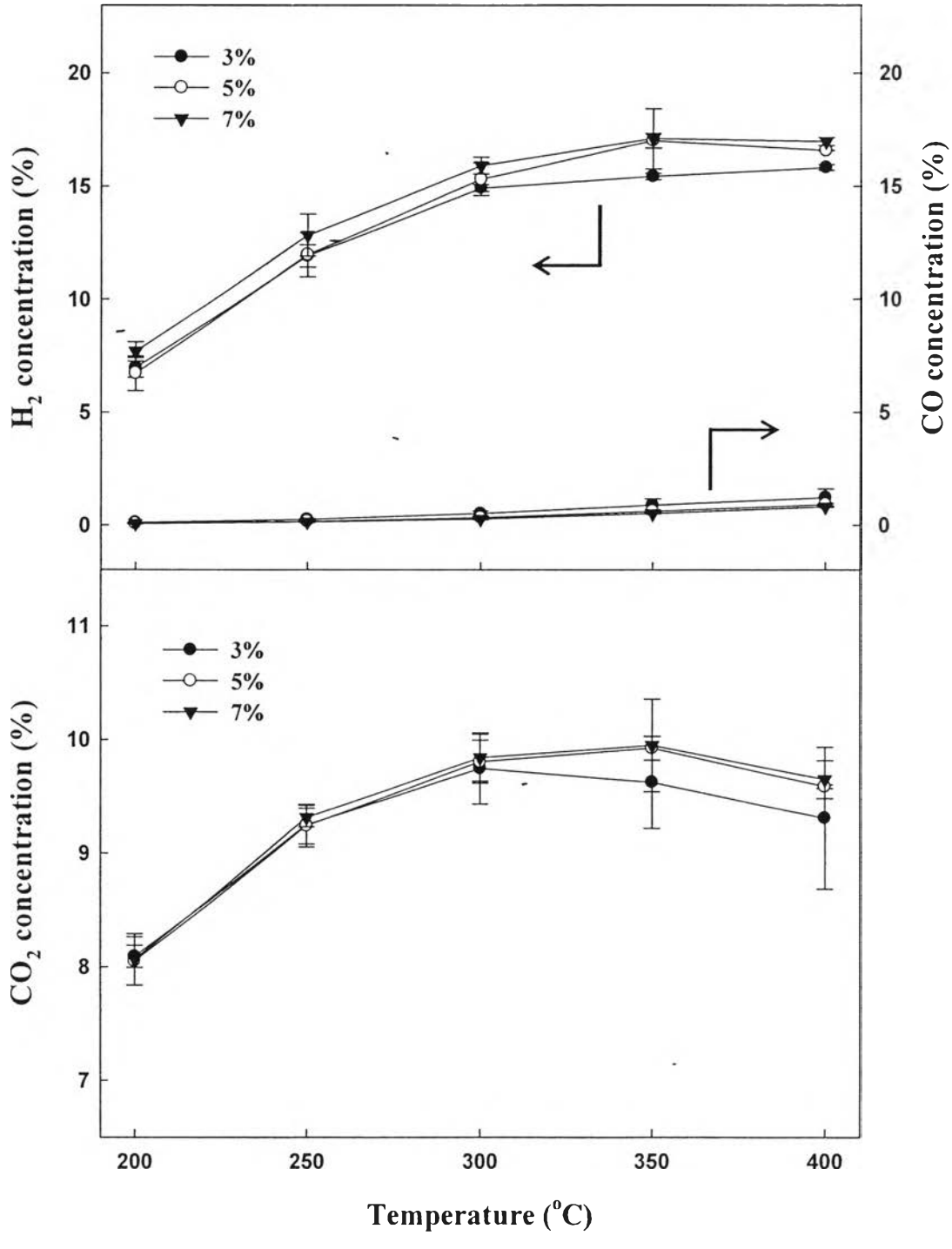

Figure 4.22 Effect of total metal loading on the concentration of H_2, CO, and CO_2 over 3Au1Cu/$Ce_{0.75}Zr_{0.25}O_2$ catalysts calcined at 400 °C (Reaction conditions: $O_2/H_2O/CH_3OH$ molar ratio = 0.6:2:1).

4.2.6 Effect of Calcination Temperature of Catalyst on Catalytic Performance

To study the effect of calcination temperature of 3Au1Cu/$Ce_{0.75}Zr_{0.25}O_2$ catalysts with 5 wt% total metal loading on catalytic performance. The calcination temperatures were varied at 200, 300, and 400 °C.

Sandoval *et al.* (2013) reported that the temperature of activation in air had an important role on the catalytic activity of catalysts. Figure 4.23 shows the methanol conversion and hydrogen yield from various catalysts. The results showed that the 3Au1Cu/$Ce_{0.75}Zr_{0.25}O_2$ catalyst calcined at 300 °C exhibited the best catalytic activity. This may be related to the metal content in catalyst, as shown in Table 4.1. The gold content of catalysts, which calcined at 200, 300, and 400 °C, were 4.12, 4.45, and 4.30, respectively. These contents may be correlated to the catalytic activity of catalysts. Furthermore, the TPR profiles in Figure 4.7C showed that the peaks of reduction were shifted to higher temperature as the calcination temperature increase. The shift is corresponded to the larger size of alloy particle and the improvement of alloy–support interaction. This result was in accordance with Sandoval *et al.* (2013). The catalyst calcined at 300 °C showed a strong uptake of hydrogen at ~110 °C, which attributed to the presence of more active site (Llorca *et al.*, 2008). Therefore, the more active site brought 3Au1Cu/$Ce_{0.75}Zr_{0.25}O_2$ catalyst calcined at 300 °C to exhibit the best catalytic activity over other catalysts. Moreover, the gas concentration of H_2, CO, and CO_2 also reported in Figure 4.24.

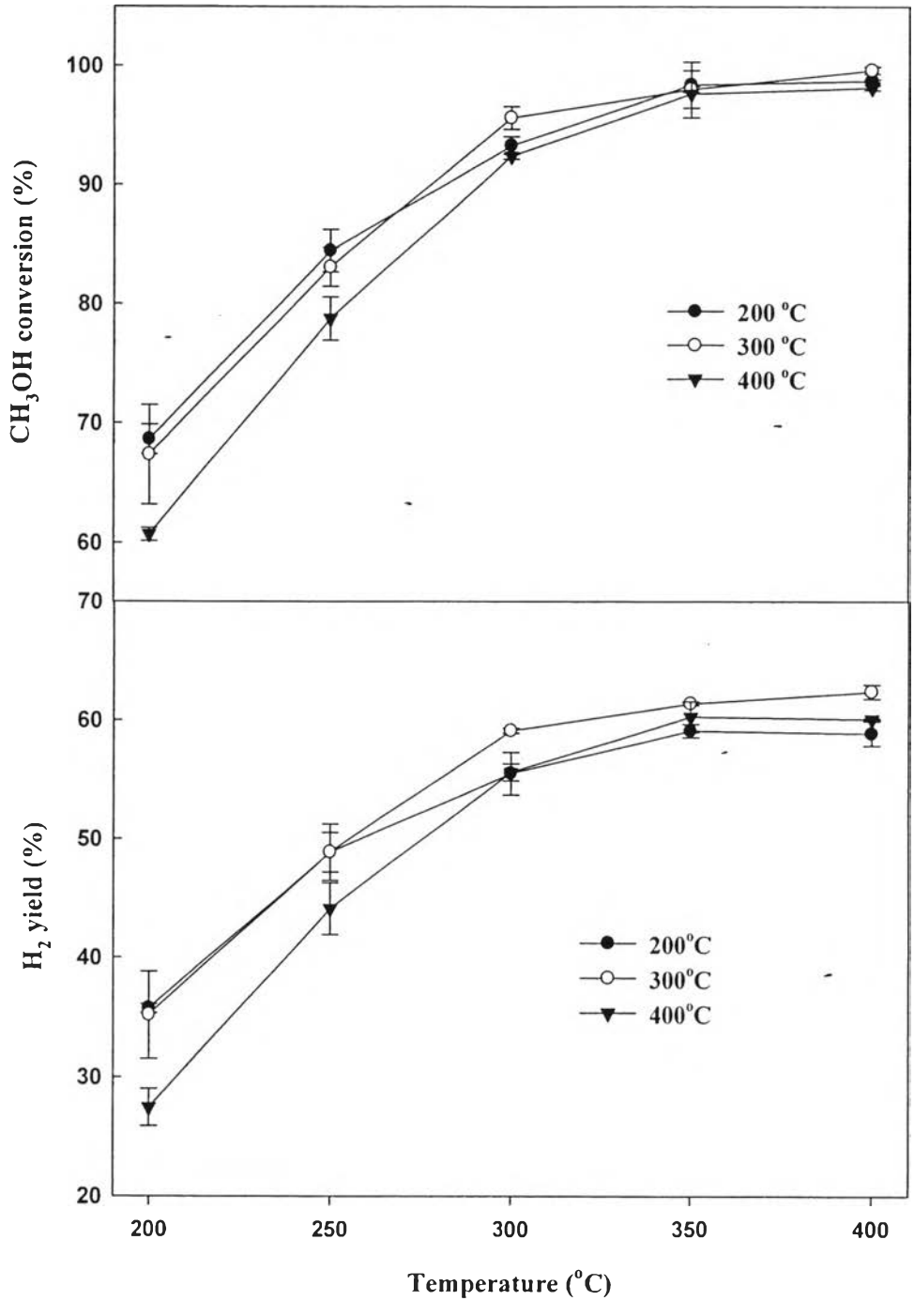

Figure 4.23 Effect of calcination temperature on the methanol conversion and hydrogen yield over 3Au1Cu/$Ce_{0.75}Zr_{0.25}O_2$ catalysts; total metal loading = 5 wt% (Reaction conditions: $O_2/H_2O/CH_3OH$ molar ratio = 0.6:2:1).

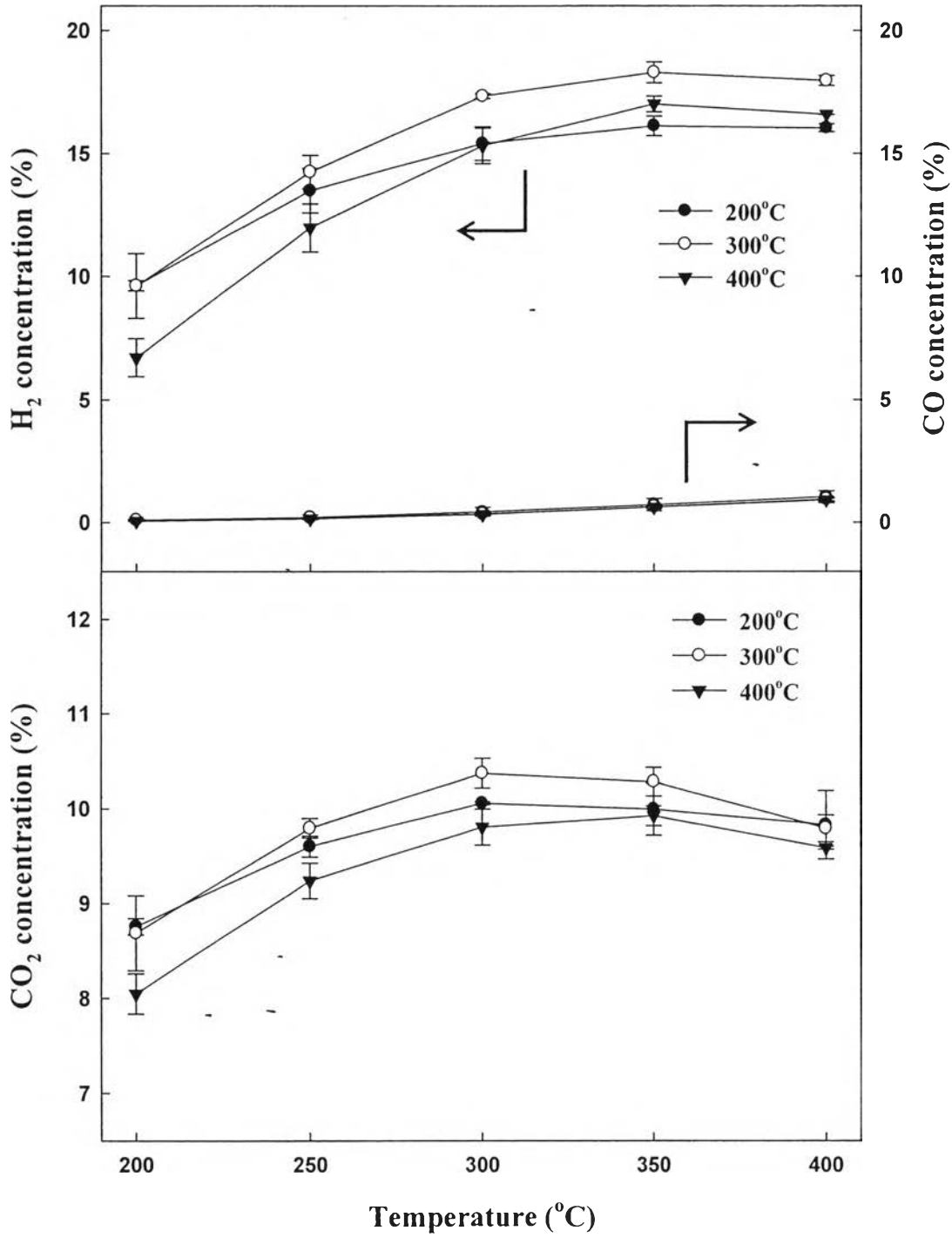

Figure 4.24 Effect of calcination temperature on H_2, CO, and CO_2 selectivity over 3Au1Cu/$Ce_{0.75}Zr_{0.25}O_2$ catalysts; total metal loading = 5 wt% (Reaction conditions: $O_2/H_2O/CH_3OH$ molar ratio = 0.6:2:1).

4.2.7 Effect of Side Reactions

It has been reported that many reactions occurred during the oxidative steam reforming of methanol (OSRM) such as steam reforming of methanol (SRM) (Eq. 4.1) and methanol decomposition (DM) reaction (Eq. 4.2) (Turco *et al.*, 2004). Therefore, it was necessary to study the effect of side reactions over the 3Au1Cu/$Ce_{0.75}Zr_{0.25}O_2$ calcined at 300 °C with total metal loading 5 wt%.

$$CH_3OH + H_2O \rightarrow CO_2 + 3H_2 \quad , \Delta H^{o}_{298} = +49.4 \text{ kJmol}^{-1} \qquad (4.1)$$

$$CH_3OH \rightarrow CO + H_2 \qquad \Delta H^{0}_{298} = +92.0 \text{ kJmol}^{-1} \qquad (4.2)$$

The 5 wt% of 3Au1Cu/$Ce_{0.75}Zr_{0.25}O_2$ catalyst calcined at 300 °C was tested. The reaction conditions were operated at 0.8 ml/hour of liquid flow rate for DM testing, 50 ml/min of carrier gas (He), and reaction temperature range of 200 to 400 °C. Figure 4.25 shows the methanol conversion and hydrogen yield for OSRM, SRM, and DM reactions. It can be seen that the OSRM reaction exhibited the highest catalytic activity over whole range of reaction temperature, whereas the SRM reaction drastically increased at high temperature (350–400 °C). In case of DM reaction, the catalytic activity slightly increased. So, it can be concluded that the 5 wt% of 3Au1Cu/$Ce_{0.75}Zr_{0.25}O_2$ catalyst calcined at 300 °C was active for both steam reforming of methanol and decomposition of methanol reactions.

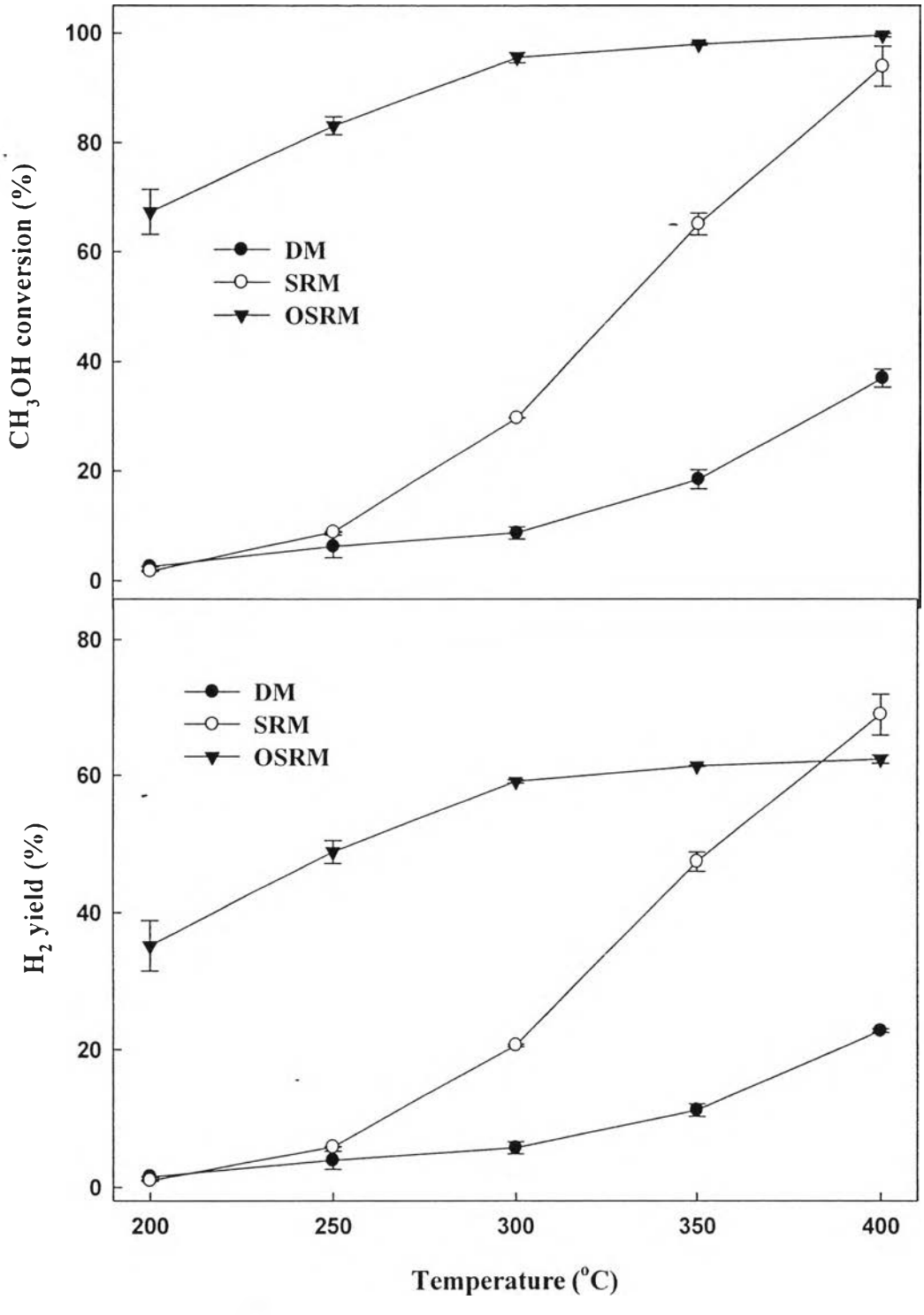

Figure 4.25 Effect of side reactions on the methanol conversion and hydrogen yield over 3Au1Cu/$Ce_{0.75}Zr_{0.25}O_2$ catalysts; total metal loading = 5 wt%.

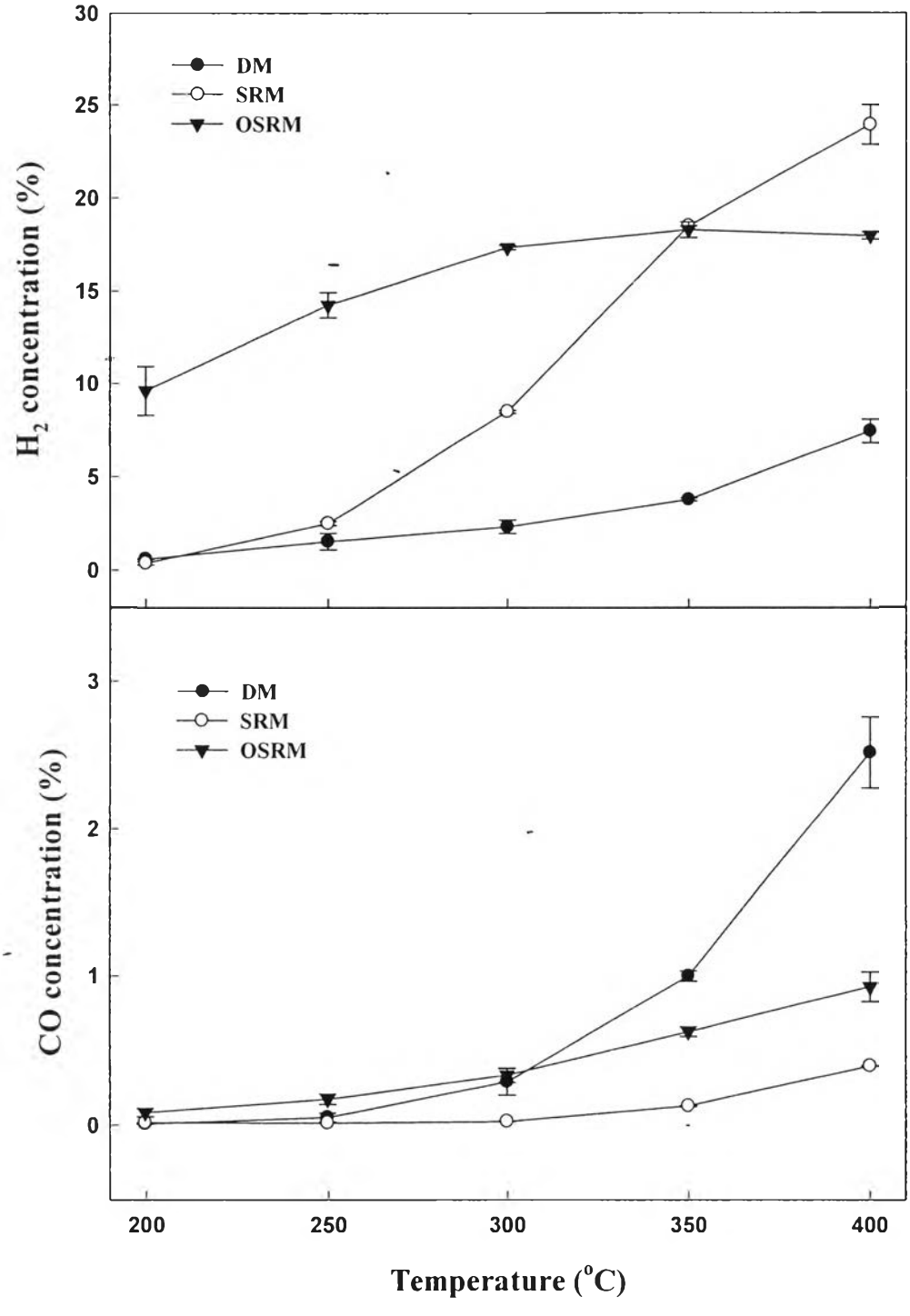

Figure 4.26 Effect of side reactions on the concentration of H_2 and CO over 3Au1Cu/$Ce_{0.75}Zr_{0.25}O_2$ catalysts; total metal loading = 5 wt%.